Chemistry–A European Journal
Research Article
doi.org/10.1002/chem.202400669
Chemistry Europe
European Chemical Societies Publishing
www.chemeurj.org

Probing Basal and Prismatic Planes of Graphitic Materials for Metal Single Atom and Subnanometer Cluster Stabilization

Mathieu Vidal[+],[a] Jyoti Pandey[+],[b] Javier Navarro-Ruiz[+],[c] Joris Langlois,[a, d] Yann Tison,[e] Takeharu Yoshii,[f] Keigo Wakabayashi,[f] Hirotomo Nishihara,[f] Anatoly I. Frenkel,[g, h] Eli Stavitski,[h] Martine Urrutigoïty,[a] Cristian H. Campos,[i] Cyril Godard,[d] Tobias Placke,[j] Iker del Rosal,[c] Iann C. Gerber,[c] Valeri Petkov,[b] and Philippe Serp*[a]

Supported metal single atom catalysis is a dynamic research area in catalysis science combining the advantages of homogeneous and heterogeneous catalysis. Understanding the interactions between metal single atoms and the support constitutes a challenge facing the development of such catalysts, since these interactions are essential in optimizing the catalytic performance. For conventional carbon supports, two types of surfaces can contribute to single atom stabilization: the basal planes and the prismatic surface; both of which can be decorated by defects and surface oxygen groups. To date, most studies on carbon-supported single atom catalysts focused on nitrogen-doped carbons, which, unlike classic carbon materials, have a fairly well-defined chemical environment. Herein we report the synthesis, characterization and modeling of rhodium single atom catalysts supported on carbon materials presenting distinct concentrations of surface oxygen groups and basal/prismatic surface area. The influence of these parameters on the speciation of the Rh species, their coordination and ultimately on their catalytic performance in hydrogenation and hydroformylation reactions is analyzed. The results obtained show that catalysis itself is an interesting tool for the fine characterization of these materials, for which the detection of small quantities of metal clusters remains a challenge, even when combining several cutting-edge analytical methods.

Introduction

Catalysis is an interdisciplinary key technology in which supported metal catalysts dominate the production technology of chemicals, fuels and polymers, and are the key to environmental protection. As the active phase is often composed of noble metals, expensive and mostly identified as critical elements, a logical step is to optimize their dispersion on the support. Supported single-atom metal catalysts (SACs) can achieve maximum metal dispersion. A SAC contains only isolated single metal atoms embedded on a support.[1] Versatile applications of this type of catalysts have already been reported in organic synthesis, environmental remediation, energy conversion, and biomedicine.[2] For such catalysts, an environment preventing the migration of the single atoms to the surface accomplishes stabilization. Thus, multiple coordination generally occurs with a strong covalent bonding of the single metal atom to the support, leading to catalysts that can be very robust[3] and usable in industrial processes.[4] The absence of ensemble effects in SACs and the charge transfer to or from the support significantly affect adsorption and induce different reactivity compared to metallic particles/clusters. Consequently,

[a] M. Vidal,[+] J. Langlois, M. Urrutigoïty, P. Serp
Laboratoire de Chimie de Coordination (LCC) UPR 8241 CNRS, Toulouse INP Université de Toulouse LCC, composante ENSIACET, 4 allée Emile Monso, F-31030 Toulouse, France
E-mail: philippe.serp@ensiacet.fr

[b] J. Pandey,[+] V. Petkov
Department of Physics Central Michigan University Dow Hall 203, MI 48859 Mount Pleasant, USA

[c] J. Navarro-Ruiz,[+] I. del Rosal, I. C. Gerber
LPCNO, INSA – CNRS – UPS Université de Toulouse 135 Avenue de Rangueil, F-31077 Toulouse, France

[d] J. Langlois, C. Godard
Departament de Química Física i Inorgánica Universitat Rovira i Virgili Carrer de Marcel·lí Domingo 1, 43007 Tarragona, Spain

[e] Y. Tison
Université de Pau et des Pays de l'Adour E2S UPPA, CNRS, IPREM, 64000,Pau, France

[f] T. Yoshii, K. Wakabayashi, H. Nishihara
Advanced Institute for Materials Research/Institute of Multidisciplinary Research for Advanced Materials Tohoku University 2-1-1 Katahira, Aoba Ward, 980-8577 Sendai Miyagi, Japan

[g] A. I. Frenkel
Department of Materials Science and Chemical Engineering Stony Brook University Stony Brook, 11794 New York, USA

[h] A. I. Frenkel, E. Stavitski
National Synchrotron Light Source (E. Stavitski) and Chemistry Division (A. I. Frenkel) Brookhaven National Laboratory 11973 New York, USA

[i] C. H. Campos
Departamento de Físico-Química Facultad de Ciencias Químicas Universidad de Concepción, Edmundo Larenas 129, Casilla 160-C Concepción, Chile

[j] T. Placke
MEET Battery Research Center University of Münster Corrensstraße 46, 48149 Münster, Germany

[+] These authors have equally contributed to this work.

Supporting information for this article is available on the WWW under https://doi.org/10.1002/chem.202400669

SACs may offer high reactivity and selectivity towards some reactions, provided their electronic properties are correctly tuned.[5] Therefore, it is mandatory to probe and tune the coordination environment in SACs to reach high catalytic performance in terms of activity, selectivity, and stability. Information on the symmetry, oxidation state, local coordination, and structural and electronic properties of the metal single atom is usually obtained by combining different analytical techniques, such as aberration-corrected high-angle annular dark-field scanning transmission electron microscopy (AC HAADF-STEM), X-ray absorption spectroscopy (XAS), X-ray photoelectron spectroscopy (XPS), and diffuse reflectance infrared Fourier transform spectroscopy (DRIFTS), coupled to computational studies.[6]

The range of support materials for SACs has expanded from metal (hydr)oxide/nitride/carbide/sulfide to metals and carbon materials.[7] Among the several types of supported SACs, carbon-supported SACs have received much attention because the structure of the carbon (nano)material as well as its surface chemistry, although sometime complex, can be tuned and exploited for the stabilization and reactivity of the SACs,[8] allowing applications in thermal-, photo-, and electrocatalysis.[9] Precise understanding of metal single atom anchoring modes on carbon materials and potentially their engineering are key issues for obtaining new catalytic properties. In general, the carbon materials used in catalysis exhibit a high carbon content with sp^2 hybridization (graphitic structure). Different kinds of defects are present on these surfaces that are able of stabilizing metal single atoms. The surface chemistry of sp^2-type carbon material is mainly dictated by: (i) basal and edge carbon atoms and (ii) point defects such as structural carbon vacancies or non-aromatic rings.[10] These imperfections and defects along the edges of the graphene layers are the most active sites owing to high densities of unpaired electrons. Since these carbon materials are usually produced from hydrocarbons, the dangling bonds at the edges of the carbon layers are mostly saturated by hydrogen atoms. Many modeling studies have shown that metal single atoms can be stabilized by vacancies or edges,[11] including H-terminated edges at which H atoms can desorb to allow adsorbed metal atoms to find stable positions (inverse hydrogen spillover).[12] If both *sp*- and sp^2-hybridization of carbon atoms exists, such as in graphdiyne, meta single atom stabilization is also possible.[13] In addition, oxygen-containing functional groups (OFGs) are the most common functionalities present on the carbon surface and carbon surface oxidation is the most popular form of carbon surface modifications.[14] Oxygen atoms are bound to the defects and form various surface OFGs (carboxylic acids, anhydrides, lactones, phenols, carbonyls, ethers) requiring the combination of multiple analysis techniques to obtain a meaningful qualitative and quantitative assessment of the different surface species.[15] These OFGs have been identified as potential sites for the stabilization of metal species,[11a,16] including metal single atoms.[17] Alternatively, substitutive doping of heteroatoms to various carbon materials has also attracted attention as one of the possible techniques to improve the electronic and chemical properties of carbon.[18] Among them, nitrogen is particularly appealing due to its chemical versatility and the induced doping produced by a single N/C substitution.[19] Beside N-doped carbon materials,[20] graphitic carbon nitride[21] also emerges as a unique support for preparing SACs due to the presence of N-rich macro-heterocycles in the lattice, which can firmly anchor metal atoms.[22] These N-containing materials offer relatively good control of the coordination sphere of isolated atoms. Finally, although the defect-free graphitic basal surface is not capable of stabilizing metal single atoms,[11a] the intercalation of transition metal single atoms into graphite was reported many years ago.[23] In these latter structures, metal atoms form π-type complexes, where the carbon support acts as a polydentate aromatic ligand.

Surprisingly, although: (i) the most common sites for stabilizing metal single atoms on common carbon materials arise from intrinsic and oxygen-containing defects, and (ii) commercial carbon-supported catalysts contain supported metal single atoms,[24] currently N-coordinated metals with prominent coordination of porphyrin type M-N_4 are almost exclusively examples of SACs on carbon surfaces. Until now, few work has been devoted to understanding the local electronic states and coordination environment of metal single atoms on carbon materials containing intrinsic and oxygen-containing defects.[25] It should be noted that in some of these works the possible presence of OFGs is not taken into account and that the coordination of single atoms is limited to an M–C_n environment (atoms isolated in a monovacancy[25e–g,i,l] or on the edges[25k]). However, the existence of these single vacancies under ambient conditions is questionable since the dissociation of O_2 on such point defects is barrierless.[26] In addition, some work is generally performed with model supports mainly containing one type of stabilization defects. Thus, for a Co_{SA}/G catalyst (G = graphene exposed to ozone to produce uniform epoxy functional groups) a six-coordinated structure (Co_{SA}-O_2C_4) was proposed based on DFT calculations in combination with EXAFS experiments, wherein individual Co atoms are bonded to two interfacial O atoms and four C atoms.[25a] Similarly, Lu and coworkers considered only the presence of phenolic groups (based on XPS analysis) in their studies on Pd SACs on graphene.[25d,j] Amal and coworkers investigated the direct environment of Pt_{SA} anchored at the edges of edge-rich vertically aligned graphene decorated with few OFGs of the same type.[25b] They found an optimized Pt structure with a coordination number of 4 by anchoring Pt to two O atoms in the upper graphene layer and two C atoms in the lower layer. Obviously, these studies do not take into account the rich and complex surface chemistry of O-containing and intrinsic defects-containing carbon materials.

In this study, the local electronic states and coordination environment of rhodium single atoms stabilized by carbon materials exhibiting different proportion of basal and prismatic planes are investigated. The resulting SACs have no additional ligands bonded to the metal center and the single atoms are truly bonded to the support through covalent interactions. Four carbon supports were used, including carbon nanotubes (CNTs), few-layer graphene (FLG), carbon nanofibers (CNFs, fishbone type), and a fibrous material (FM) featuring a highly disordered

surface structure. The supports were subjected to surface oxidation to introduce various OFGs. Complementary techniques, including AC HAADF-STEM, XPS, and XAS analysis, are employed to understand the nature of active sites at the atomic level. The objective is also to investigate the influence of local coordination on the reactivity of these materials, which have been evaluated for hydrogenation and hydroformylation reactions. This study demonstrates that the basal surface/prismatic surface ratio of the carbon support has a major effect on the synthesized catalysts and their performance. Furthermore, it is shown that the detection of small quantities of metal clusters in these samples is not easy, even by combining cutting-edge analytical methods. Only the study of reactivity in catalysis can allow the detection of these species.

Results and Discussion

Carbon Support Characterization

CNTs, FLG, CNFs, and FM were used as carbon support. As the ratio between basal plane and prismatic surface areas is expected to be an important factor in determining the surface reactivity of these materials,[25k,27] DFT calculations derived from N_2 adsorption data were used to determine the surface heterogeneity by adsorption potential distribution.[28] The absolute and relative extent of non-basal plane surfaces (= accumulated prismatic surfaces and defect surfaces) and basal plane surfaces were quantified (Table S1). The defect surface consists of surface steps and/or OFGs.[28a] Among all materials, FM does not show any basal plane surface. The relative extent of the surface area of the basal plane follows the order CNTs > FLG > CNFs > FM. Since the accuracy of this approach for probing basal and prismatic surface areas may be limited,[29] we also rely on a recently developed, high-temperature programmed desorption method (HT-TPD, up to 1800 °C), which allows a quantitative evaluation of edges with high accuracy by measuring evolved gases.[30] The two methods (DFT calculations derived from N_2 adsorption data and HT-TPD) were compared. The TPD profiles obtained for all samples are shown in Figure S1. CO, CO_2, H_2O, and H_2 were detected due to the thermal decomposition of OFGs and H-terminated edge sites. Using the number of edge sites, the surface area of the edge sites (S_{edge}) was calculated. The values obtained from HT-TPD (S_{edge}, Table S2) and from N_2 adsorption ($S_{prismatic}$ Table S2), although different, as HT-TPD can detect hidden edge sites not available for N_2 adsorption, follow exactly the same trend (Figure S2). These experiments confirm that both methods can be used to probe the prismatic surface in these graphitic carbon materials.

The four materials were oxidized with nitric acid to increase the concentration of OFGs, which can act as anchoring sites for the metal atoms.[8] The low- and high-resolution TEM micrographs of the samples are shown in Figure S3 and Figure 1, respectively. The FLG presents between four and ten layers of graphene, consistent with its relatively low surface area (S_{BET} = 41 $m^2 g^{-1}$, S_{DFT} = 47 $m^2 g^{-1}$). The CNTs (S_{BET} = 199 $m^2 g^{-1}$, S_{DFT} = 206 $m^2 g^{-1}$) have an external diameter of around 15 nm and present graphene layers parallel to the axis of the tube. The oxidation by HNO_3 has created defects on their surface.[31] The CNFs (S_{BET} = 148 $m^2 g^{-1}$, S_{DFT} = 176 $m^2 g^{-1}$) have an external diameter of about 150 nm and their graphene layers show an angle of approximately 30° with respect to the fiber axis. Most of the edges are open and few closed loops are visible. The FM (S_{BET} = 192 $m^2 g^{-1}$ S_{DFT} = 274 $m^2 g^{-1}$) contains fibers of various diameters (50–200 nm) showing a highly disordered surface with many open edges.

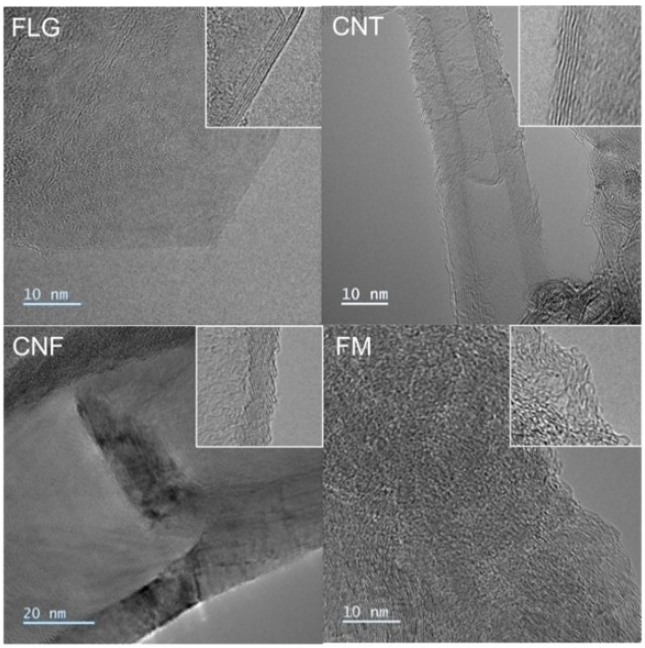

Figure 1. HRTEM micrographs of the four supports. Scale bar = 10 nm (FLG, CNTs, FM) and 20 nm (CNFs).

Results of Raman and XRD characterization of the materials are given in Table S3. A commonly calculated parameter to assess the structural disorder in carbon materials is the ratio between the integrated intensities of the Raman D band (I_D) at~1380 cm^{-1} (reflecting graphitic structure defects) and the Raman G band (I_G) at~1580 cm^{-1} (reflecting the graphitic ordered structure).

The FLG shows the lowest I_D/I_G ratio, consistent with a low structural disorder, while the CNTs and FM show the highest ratio, while the CNFs shows an intermediate value for the intensity ration that is consistent with a modest degree of structural disorder. These results suggest that the structural distortion, D, due to defects in the studied materials may be ranked as follows: $D(FLG) < D(CNF_S) < D(CNTs) \approx D(FM)$. It is worth noting that the defects caused by OFGs do not have a significant footprint in the Raman spectra. The interlayer distance (d_{002}) and crystallite size values L_c (crystallite stack height of the stack of graphitic layers) and L_a (width of the stack of graphitic layers) were determined by XRD (Table S3). All materials present an interlayer distance close to 0.34 nm, which is slightly higher than that of perfect graphite (0.335 nm), where that distance appears shorter for FLG and CNFs. On the other

hand, FLG shows the largest values for L_c and L_a, followed by CNFs. Together, the values of d_{002}, L_c and L_a, point to the following degree of crystallinity: FLG > CNFs > CNTs ≈ FM, consistent with the Raman data (Figure S4).

The reactivity of these materials toward air oxidation was probed by TGA (Table S3). The maximum decomposition rate temperature of the four supports follows the order FLG > CNTs > FM > CNFs, pointing to the higher reactivity of carbon materials presenting surface edges. As HNO_3 treatment significantly increases the amount of OFGs, XPS analyses were performed to probe the surface chemistry of the supports. The surface oxygen content determined by XPS follows the order FLG < CNTs < CNFs < FM (Table S3). This oxygen content and degree of crystallinity do not seem to be correlated, but the former is expected to be correlated with the prismatic surface area (*vide infra*). The XPS spectra were fitted with an analytical function including three components (Figure S5 and Table S4). These components were assigned to C=O groups (component I 531.3–531.5 eV, including carbonyl, lactone, and carboxylic groups), C–OH and/or C–O–C groups (component II, 533.1–533.3 eV, ether and hydroxyl groups bonded to aromatic/aliphatic), and chemisorbed water/oxygen sub monolayer (component III, 535.0–536.1 eV).[32] The C=O/C–O ratio varies from 0.8–1.2 between the different samples. Previous investigation by Sherwood has indicated that the valence band region is more sensitive to changes in the surface chemical environment than the core level.[33] Separation of the mainly O*2 s* feature peak from the C*2 s* peak in the valence band can be used to determine the nature of the surface groups.[34] It was determined that the C–OH–type groups produces the lowest separations between the O*2 s* and C*2 s* peaks, while the CO, –C–O–C–, and COOH groups show higher separations.[35] The valence band spectra for the four samples are shown in Figure S6. The spectra show an intense peak at 18 eV indicating a significant amount of C *2 s* intensity, which is expected for carbon materials. In addition, there is also a peak at ~25 eV, corresponding to an orbital of O *2 s* character. The O *2 s*-C *2 s* peak separation for FM is higher (~11 eV) than that for the other three samples (~7 eV), including CNF. The separations and the analysis of the O 1s region (similar C=O/C–O ratio for FM and CNF) indicate that the FM sample is likely to contain significantly more –C–O–C– OFGs than the CNF sample.

DFT calculations and data for N_2 absorption were used to determine the surface heterogeneity by N_2 adsorption potential distribution. Representative distributions of the adsorption potential of the four supports, calculated from the N_2 adsorption data, are displayed in Figure S7. The absolute and relative extent of non-basal plane and basal plane surfaces were quantified (Table S5). Among all materials, FM does not show any basal plane surface. The absolute and relative extent of the surface area of the non-basal plane follows the order FM > CNFs > CNTs > FLG. This order is consistent with the surface oxygen content determined by XPS (Figure S8), and confirms the higher chemical reactivity of the prismatic surface. CNTs and FLG show a higher degree of defect surface than CNFs and FM do. This could be due to the generation of a large number of vacancies on the FLG and CNT surface during the oxidation treatment,[31] which could contribute to the defect surface (Figure S7).

The characterizations of the oxidized supports reveal several points that should be important for the stabilization of metal single atoms. First, the DFT computed surface area of these materials differs, with the FLG showing the lowest surface area. Secondly, the prismatic surface area, which is the most reactive, varies significantly between the supports. Finally, the number of OFGs varies in the same way as the prismatic surface area of the supports. These carbon support features are reported in Table 1.

Supported Rh Catalyst Synthesis and Characterization

To understand the nature of active sites at the atomic level, techniques such as ICP, AC HAADF-STEM, TPD, XPS, and DFT-assisted XAS analysis were employed. Four different carbon-supported rhodium catalysts with a nominal Rh loading of 1% w/w were prepared on the oxidized supports. To produce rhodium catalysts containing primarily Rh_{SA}, a thermochemical process was used to create vacancies on the carbon supports by selectively removing carboxylic groups.[36] These defective supports were then used to deposit 1% w/w Rh from the tris(allyl)rhodium precursor by impregnation in pentane under an inert atmosphere. The final carbon-supported rhodium catalysts were obtained after low-temperature reduction with H_2 (Figure S9). The impregnation method has already been successfully used for the preparation of ultradispersed rhodium-based catalysts.[37] The effective Rh loading in these samples was determined by ICP-OES (Table 2) and found to be different in the different samples. Good correlations were found between the effective Rh loading and the prismatic surface area determined by DFT calculations using data for N_2 adsorption or data for the atomic % of oxygen determined by XPS (Figure S10).

Low- and high-resolution AC HAADF-STEM images of the samples are shown in Figure S11 and Figure 2, respectively. Rh_{SA} can be seen in all samples. However, the presence of Rh clusters is also visible in the Rh/FLG sample (Figure S11) and, to a lesser extent, in the CNT sample (Figure S11 and Figure S12). The Rh cluster size distributions for these two samples are shown in Figure S13. The mean size of the Rh cluster (Rh_{NP}) is decreasing from 0.7 nm in Rh/FLG to 0.5 nm in Rh/CNT (Table 2). This size difference was attributed to the higher prismatic surface area and oxygen content for the CNT support, which should

Table 1. Main textural and surface properties relative to metal single atom stabilization of the four carbon supports.

Support	Textural properties		XPS
	DFT surface area ($m^2 g^{-1}$)	$S_{prismatic}$ ($m^2 g^{-1}$)	%O
FLG	47	15	4.2
CNT	206	83	6.4
CNF	176	130	12.7
FM	274	274	15.9

Table 2. ICP, XPS and STEM results for the four carbon-supported Rh catalysts.

Sample	Rh loading (%)[a]	Surface Rh (at. %)[b]	Rh cluster size (nm)	Rh_{SA}/Rh_{NP} ratio	Rh_{SA}/Rh_{total}	
					STEM	XPS
Rh/FLG	0.13	0.8	0.74 ± 0.25	9	0.31	0.62
Rh/CNT	0.6	0.4	0.55 ± 0.17	23	0.75	1
Rh/CNF	0.8	0.3	not detected	–	~1	1
Rh/FM	1	0.3	not detected	–	~1	1

[a] From ICP analyses. [b] From XPS analyses.

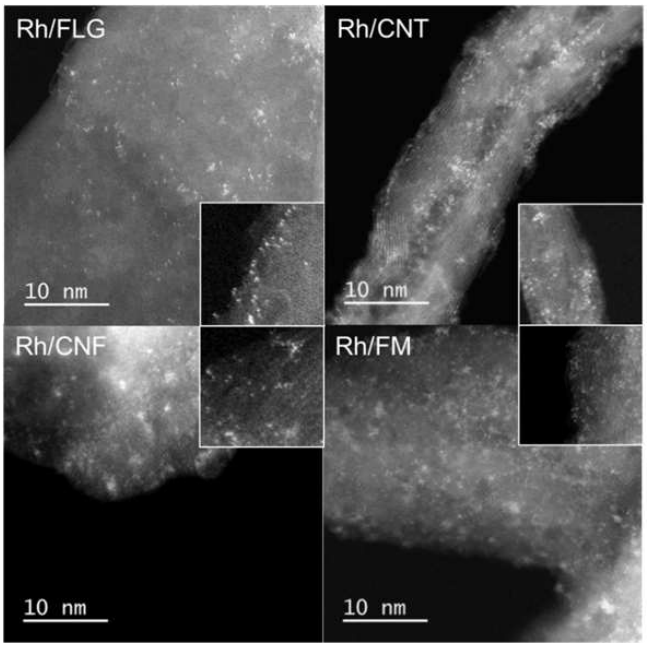

Figure 2. AC HAADF-STEM micrographs of the four carbon-supported Rh catalysts (scale bar = 10 nm).

contribute to a higher metal dispersion. The Rh_{SA}/Rh_{NP} ratio (a number ratio) was measured for these two samples from HAADF-STEM analyses of at least 1000 elements. It was 9 and 23 for Rh/FLG and Rh/CNT, respectively. This corresponds to an atomic % of Rh_{SA} relative to the total Rh ($Rh_{SA} + Rh_{NP}$) determined by HAADF-STEM[38] of 31% and 75% for Rh/FLG and Rh/CNT, respectively (Table 2). For the other two samples, although the presence of few small Rh clusters cannot be excluded (particularly for the Rh/CNF sample, Figure S14), STEM analyses do not help reveal them unambiguously, because these samples are thicker and the density of Rh_{SA} is quite high.

XPS analyses were performed on all four samples with introduction of the samples *via* an Ar-filled transfer vessel from a glove box under a controlled argon atmosphere, being able to exclude any air oxidation. Figure S15 shows the deconvolution of the high-resolution O 1s spectra of the four catalysts (the deconvolution results are given in Table S6). For all four catalysts the O 1s core peaks are composed of two contributions at approximately 531.5 eV and 533.0 eV, they are respectively assigned to C=O and C–O bonds. No signs of Rh–O bonds (expected at approximately 530 eV) are observed here, which is not surprising considering the low concentration of Rh.

Due to the thermochemical process used for the preparation of the catalyst, adsorbed water or carboxylic groups were not observed as on the bare supports, and the C/O ratio is higher than for the bare supports (Table S3). The C=O/C–O ratio is higher for the Rh/CNT sample (1.3) than for the other samples (0.5–0.75). The valence band spectra of the four catalysts are shown in Figure S16a. As for the bare supports, the O *2 s*-C *2 s* separation of Rh/FM is significantly higher (10.2 eV) than that for the other three samples (7.6 eV). Figure 3 shows the deconvolution of the high-resolution Rh *3d* spectra of the four catalysts (deconvolution results are given in Table S7). The high-resolution Rh *3d* XPS spectrum of Rh/FLG contains two broad peaks corresponding to the Rh $3d_{5/2}$ and $3d_{3/2}$ states of the spin-orbital splitting (they were fitted using two doublets). The peaks at 307.4 eV and 312.1 eV and the energy splitting value of 4.7 eV correspond to metallic Rh_{NP} on FLG (Rh $3d_{5/2} = 307.2$ eV for 1.3–3.9 nm Rh_{NP}).[39] The slight upward shift of the binding energy (BE) in Rh/FLG could be associated to charge transfer from the Rh clusters to the support, as already observed for Rh clusters deposited on CNTs,[40] and modeled for Rh clusters on graphene oxide.[41] The peaks at 309.2 eV and 315.5 eV are ascribed to oxidized Rh species. These peaks should correspond to Rh_{SA} exhibiting a strong interaction with the support (electronic interaction between the outermost orbitals of the Rh shell and the C/O of the support), with electrons transferred from Rh to the support. It is worth noting that the oxidation state of the oxidized rhodium species in Rh/FLG (BE = 309.2 eV) is close to that of Rh_2O_3 (+3), for which the rhodium $3d_{5/2}$ peak is located around 308.4–309.5 eV.[42] From this XPS analysis, the atomic % of Rh_{SA} in Rh/FLG is 62.5%, which is higher than the value obtained from HAADF-STEM analyses (Table 2).

For the other three samples, the high-resolution Rh *3d* XPS spectra do not reveal the presence of metallic Rh_{NP} and only oxidized rhodium species with BE close to those observed for Rh/FLG are detected. As STEM detected few or no Rh clusters on these samples, this provides extra evidence that the rhodium $3d_{5/2}$ peak at 309.2–309.5 eV should be due to Rh_{SA}. The BE of this peak is slightly higher for Rh/CNF and Rh/FM; *i.e.* for the two supports presenting the largest prismatic surface. At that point, it is possible to propose that the interaction of Rh_{SA} with the prismatic surface of FM and CNFs differs from that which occurs with the defective surface of FLG and CNTs. The stronger interaction of sub-nanometer Pt clusters and Pt_{SA} on CNFs

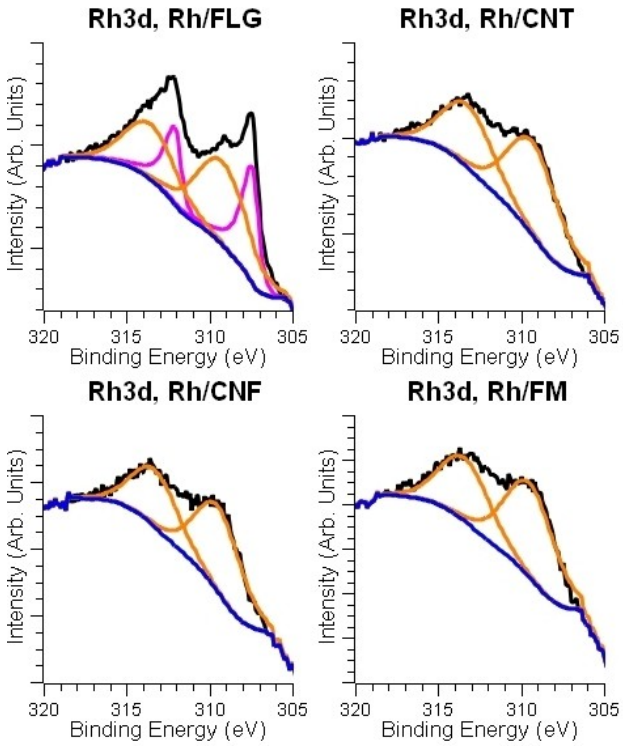

Figure 3. Core level XPS spectra of Rh *3d* for the (**a**) Rh/FM, (**b**) Rh/CNF, (**c**) Rh/CNT, and (**d**) Rh/FLG samples.

compared to CNTs have already been reported.[25k,43] It is worth noting that the surface rhodium concentration determined by XPS on the four catalysts follows an opposite order to the Rh loading determined by ICP (Table 2 and Figure S17). This could be related to the location of Rh_{SA}, which may be mainly stabilized on the defect/basal surface for FLG or on the prismatic surface for FM.

Thus, it appears that prismatic surface favors a high metal loading, whereas a defect/basal surface favors a high metal surface concentration (Figure S18). The low surface Rh concentration measured on CNFs and FM by XPS could be related to the existence of Rh_{SA} positioned at a very distant distance from the edge planes and interacting only with the carbon atoms of the basal planes in a sandwich-type structure (intercalated Rh_{SA}),[25k,44] as in Graphimet catalysts.[23a,45] It has been predicted that Rh_{SA} intercalation between graphene layers will be thermodynamically favorable in the case of Rh because of its small effective Shannon ionic radius.[46] Different intercalation mechanisms have been proposed for metal atoms, involving carbon vacancies[47] or edges.[48] We performed DFT calculations to confirm this hypothesis, but the results obtained (Figure S19) do not support such configuration and are not in accordance with experimental XAS data (*vide infra*). Another explanation of the segregation of Rh on the FLG surface is that for this support confinement of the metal in pores is not possible, whereas metal particle confinement in CNFs or CNTs has been reported.[49] Figure S16b presents the evolution of the Rh valence band, assigned to the presence of filled Rh *4d* t_{2g} states,[50] for the four catalysts (after subtracting the support contribution). The shift of the centroid of the Rh *4d* valence band towards high BE observed for Rh/CNF and Rh/FM compared to the Rh/CNT and Rh/FLG samples can be attributed to a higher atomic % of isolated Rh_{SA} in these samples or to the presence of small Rh clusters in strong interaction with the support.[51] In the catalyst series, the *d*-band center of Rh was found at 3.4 ± 0.2 eV for Rh/FLG, 3.3 ± 0.2 eV for Rh/CNT, 3.6 ± 0.2 eV for Rh/CNF, and 3.6 ± 0.2 eV for Rh/FM. These values can be correlated to the amount of OFGs on the support (Figure S20). The correlation between the *d*-band center position and the oxygen content of the support can be explained by the changes in electronic properties of the support. The decrease in the work function (Φ) of carbon supports with decreasing oxygen functionalities has been discussed in the literature.[52] For the present study, the decrease of OFGs in FLG and CNTs would progressively lower the Φ of the graphenic layer, thus increasing the difference between the Φ of Rh and that of the support.

It has been proposed that the TPD-MS profiles of carbon-supported metal catalysts can provide valuable information on the influence of OFGs on the metal grafting.[16a] Thus, it was shown in the case of Ru and Pd catalysts that metal deposition induces the formation of new CO_2 releasing groups, the decomposition of which results in the presence of narrow (catalytic decomposition) and intense peaks.[16a,53] The TPD spectra of the four air-exposed catalysts are shown in Figure S21. No signature of a Rh-catalyzed decomposition of a Rh-surface acetato ligands interface is observed. The quantity of CO emitted by the catalysts (Rh/FM > Rh/CNF~Rh/CNT > Rh/FLG) is significantly greater than that for CO_2 and H_2. We verified in the case of the Rh/FM catalyst that this quantity of emitted CO is significantly greater than that of the support alone (Figure S22). This phenomenon can be explained if we assume that a surface reconstruction operates upon air exposure of the catalyst, which should involve the rhodium species, surface carbon atoms and oxygen.[16a]

To validate the atomic dispersion of rhodium atoms in the catalysts and explore the Rh_{SA} coordination structure, X-ray absorption spectroscopy (XAS) analysis was carried out with the help of structural models established from DFT.[54] It is worth noting that the low metal loadings of SACs and the strong influence of the support render of the analysis of XAS data more difficult in comparison to the case of bulk materials.[6,54–56] Figure 4 shows the normalized X-ray absorption near edge structure (XANES) spectra obtained at the Rh K-edge for the four rhodium catalysts. The XANES spectra for a metal Rh foil and rhodium oxide are also shown in the energy range from 23220–23260 eV.

The XANES spectra for the four catalysts are different from both the Rh-foil and rhodium oxide, where Rh atoms are not oxidized and have a formal oxidation state +3, respectively. A survey of the experimental data shows that the XANES spectra of the Rh/FLG sample and Rh metal are similar, indicating that Rh atoms in the former are in a metallic state. The Rh atoms in the other 3 catalysts appear partially oxidized but not as much as Rh^{3+} atoms in Rh_2O_3. The local coordination environment of Rh atoms has also been investigated by a non-linear least

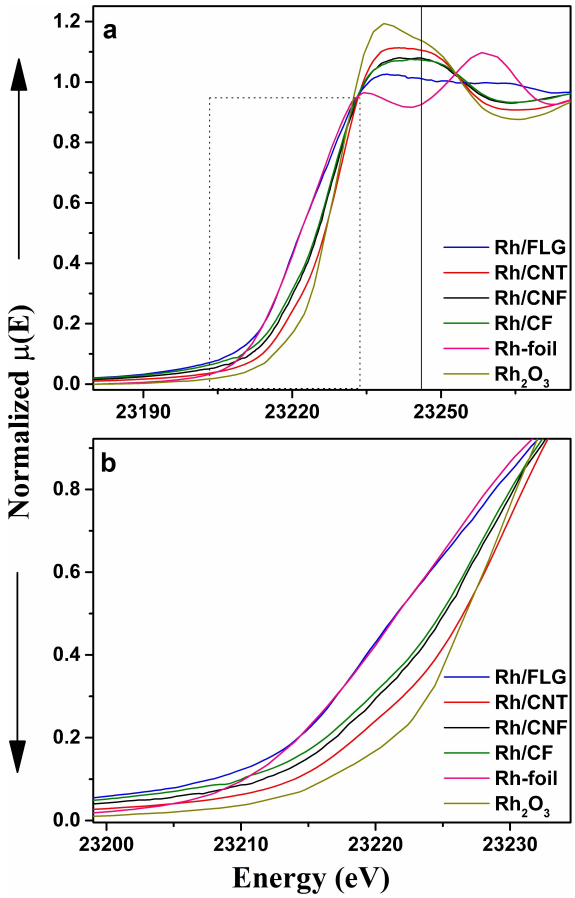

Figure 4. (a) XANES spectra of the Rh K-edge for the four carbon-supported Rh catalysts, and (**b**) selected region of the XANES spectra for better understanding of the pre-edges. All four samples exhibit pre-edges that are different from both Rh-foil and rhodium oxide.

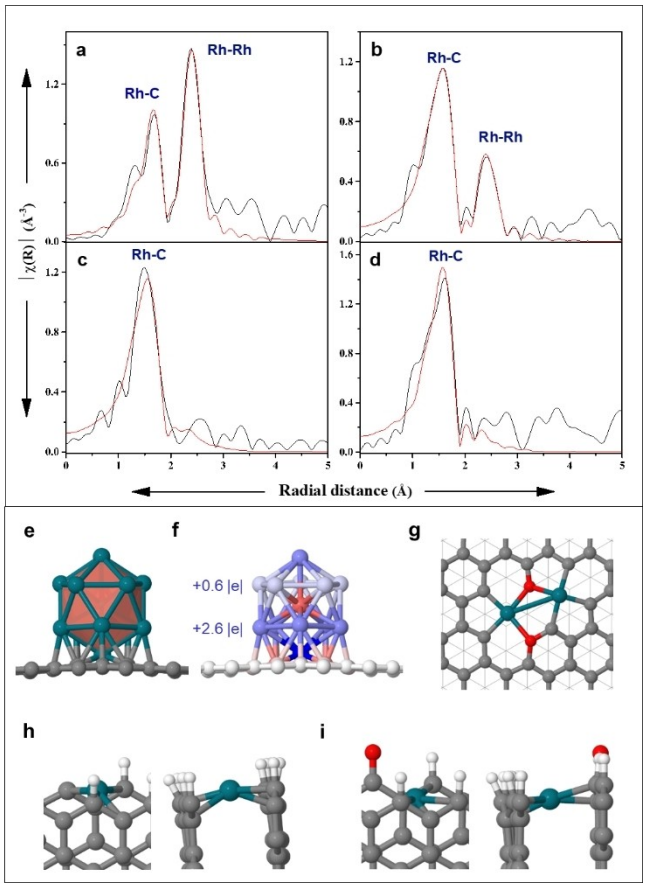

Figure 5. EXAFS fitting curves and realistic DFT models for (a, e–f) Rh/FLG, (b, g) Rh/CNT, (c, h) Rh/CNF, and (d, i) Rh/FM. The experimental and fitted EXAFS results are shown in black and red, respectively. Note that the distances in the EXAFS spectra in (a–d) are not phase corrected. The phase corrected distances are given in in Table 3. (f) Charge distribution plot (blue and red colors indicate areas of charge depletion and accumulation, respectively).

square fitting of the k^2-weighted EXAFS spectra in real space.[56] The spectra are shown in Figure S23 and Figure 5. A detailed description of EXAFS experiments and data processing can be found in refs.[57] Based upon HAADF-STEM images of the four catalysts (Figure 2), it can be expected that Rh atoms on FM and CNFs are coordinated by atoms from the carbon support alone (no Rh clusters are seen in the respective images) whereas Rh atoms on CNTs and FLG have both carbon and Rh neighbors (Rh clusters are seen in the respective images). Figure 5 shows that, of the four catalysts, the EXAFS spectra of Rh atoms in FM and CNFs exhibit two peaks, which, based on a comparison with the XAFS spectra of Rh metal and Rh_2O_3 (Figure S23), can be unambiguously attributed to the Rh–C and Rh–Rh near neighbor correlations. The results are consistent with the HAADF-STEM images. Notably, the Rh–Rh peak in the EXAFS data for Rh/FLG appears more intense in comparison with Rh–C peak, indicating the presence of Rh clusters. The Rh–Rh peak in the EXAFS data for Rh/CNT appears less intense in comparison with Rh–C peak, indicating that here Rh clusters are smaller in size/number in comparison to those in Rh/FLG. On the other hand, the EXAFS spectra for Rh/CNF and Rh/FM lack a Rh–Rh peak, indicating that these two samples include Rh_{SA} alone.

DFT generated models (see below) provided initial values for Rh–C and Rh–Rh bonding distance and coordination numbers in fitting the experimental EXAFS spectra. The fits are shown in Figure 5a–d. The resulting bonding distances and coordination numbers are summarized in Table 3. To rationalize the coordination structure of the support and the different Rh species, DFT simulations have been performed. For the design of the support presenting a greater proportion of basal planes, such as in CNTs and FLG, rhombohedral trilayer graphene (TLG) with ABC stacking order was considered. Stone-Wales (SW) defects,[58] single and multiple vacancies (SVs and MVs),[59] and/or substitutive oxygen atoms were also introduced as experimentally predicted defects (Figure S24). Previous DFT calculations have shown that vacancies, which can be present in the catalysts since they were prepared without any air exposure, and unsaturated sites are the preferred anchoring centers on carbon surfaces, exhibiting higher binding strength with metal precursors.[60] Once the different TLG have been emptied and/or O-decorated as a surface defect engineering strategy,[61] they can be used as supports for metal deposition. The experimental results provided similarities and differences about the average structural information of the species present in Rh/FLG and Rh/

Table 3. Structural parameters (distances, *R* in Å, and average coordination numbers, CN) from the EXAFS fits.

Sample	Rh–C shell			Rh–Rh shell		
	R_{exp}	R_{calc}	CN	R_{exp}	R_{calc}	CN
Rh/FLG	1.984	2.091	1.62(0.61)	2.689	2.687	2.52(0.74)
Rh/CNT	1.905	2.072	4.19(0.35)	2.715	2.715	0.69(0.15)
Rh/CNF	2.023	2.083	5.33(1.50)	–	–	–
Rh/FM	2.062	2.069	4.74(0.85)	–	–	–

CNT. Both surfaces present two shells, the first corresponding to Rh–C and the second corresponding to Rh–Rh.

No significant differences are seen for each of the bond lengths between the two surfaces. In particular, the intermetallic distance is very close to the Rh–Rh distance in the bulk metal (2.69 Å). However, the local atomic coordination differs markedly, leading to the stabilization of different Rh species. Given the low Rh–Rh CN (0.69), Rh/CNT seems to incorporate single atoms and/or dimers in close contact with the carbon plane (average Rh–C CN of 4.20). For Rh/FLG, given the higher Rh–Rh CN (2.52), it seems to incorporate Rh clusters, where only a few atoms of their surface are close to the carbon plane, resulting in a relatively low Rh–C CN of about 1.62.

For Rh/FLG, the inclusion of isolated Rh_n clusters was carried out considering n values between 3 and 13. Such models (according to their size) are representative of highly dispersed Rh catalysts (Figure S11).

The anchoring of the clusters takes place preferably on a pristine divacancy, since the Rh–C CN of about 1.62 would prevent the metal-support interaction through a single vacancy (1 V–C_3, tri-coordination) and the elimination of more than two atoms can give rise to larger and more complex defective configurations.[59] Thus, the best models in terms of energy and consistency with the EXAFS results are made up of clusters with four, five, and thirteen Rh atoms, mainly coordinated on the TLG through a vertex or one of the two exposed crystal facets, {100} and {111}. After selecting the models which were consistent with the experimental data and thermodynamically stable, the corresponding adjustment and classification is made in terms of the usual bonding distances and goodness-of-fit values and from other analytical techniques. Among the computational models that best fit the experimental data, the triangular bipyramid Rh_5 supported on a vertex (model FLG-26) and a {111} facet (models FLG-30 and FLG-31), and the icosahedral Rh_{13} supported on a vertex (model FLG-48) stand out. Despite exhibiting a slight distortion, the final clusters agree with freestanding geometric structures reported for the same cluster size,[42b,62] suggesting that being supported did not result in a significant structural alteration. In terms of stability, they present binding energies per rhodium atom between 4 and 17 kcal mol^{-1}, clearly below those calculated for the Rh/CNT models (*vide infra*). The best model in terms of energy and consistency of the experimental EXAFS data, is the Rh catalyst with the 13-atom nanocluster with distances of 2.09 Å for Rh–C and 2.69 Å for Rh–Rh. The model is shown in Figure 5e and Table 3, while the rest of the Rh/FLG models are presented in Figure S27 and Table S9.

For Rh/CNT, the anchoring of single atoms and dimers was modeled. The energetic and structural features and corresponding structures for the rhodium catalyst models are summarized in Table S10 and Figure S29, respectively. Some of the considered systems also include the presence of hydrogenated Rh species since H_2 was used as reducing agent during the synthesis process. Assuming that metallic speciation is restricted to Rh_{SA} and Rh_2, the value of 0.69 for the Rh–Rh CN requires the coexistence of both species. For the Rh_{SA} models that most closely resemble the experimental results, the anchoring sites correspond to single O-decorated vacancies and any of the divacancies. Binding energies range from 6–104 kcal mol^{-1}, with average Rh–C distances around 2.03 Å spanning mean CN of 3.0 and 4.5. But taking into account that a Rh_{SA}, regardless of the size or decoration of the vacancy it occupies, causes the absence of the Rh–Rh coordination shell (relative to the metal-metal interaction), the experimental results would show a higher proportion of dimeric species than of monomeric. Thus, omitting those with very low Rh–C CN (on the order of 2.0) or thermodynamically unstable (based on their binding energies per metal atom), the Rh_2 models that care consistent with the experimental results show 'double or quadruple vacancies, pristine (undecorated) or oxygen decorated. Therefore, the different models optimized from DFT were used to fit the experimental data and the good models were sorted out on the basis of average bonds and their distances and also goodness-of-fit values. Computational models that fit the experimental data well are those in which the dimer is located in a partially O-decorated double vacancy (2 V–C_3O_1, model CNT-14) and in pristine and partially O-decorated quadruple vacancies (4 V–C_6, models CNT-15 and CNT-16, and 4 V–C_4O_2, model CNT-17). They present high stability in terms of energy. Among them, the model CNT-17 (Rh_2 deposited in the O-decorated 4 V), with binding energies greater than 69 kcal mol^{-1} per Rh atom, structurally remarkably reproduces the presence of two peaks in the EXAFS data, turns out to fit better, with distances (2.07 Å for Rh–C and 2.72 Å for Rh–Rh) approaching those determined experimentally. This best model is depicted in Figure 5f and Table 3, while the rest of the Rh/CNT models are represented in Figure S30 and Table S11.

To design the carbon supports with the higher proportion of prismatic planes (CNFs and FM), a bilayer zigzag graphene nanoribbon (BZGNR) was used as a model. Such nanostructures exhibit unique properties, such as localized electronic states

and spins, with magnetic properties.[63] The symmetric and asymmetric H-terminated models were evaluated to provide a comprehensive view of the AB/AC stacking boundaries in bilayer graphene nanoribbon (Figures S31a–d). Structurally, the ribbon pairs exhibit a very small but notable curvature, with average ribbon-to-ribbon distances ranging between 3.50–3.56 Å, substantially longer than the characteristic 3.35 Å in graphite. At different edges, the bilayers show magnetic properties in the antiferromagnetic state, as for single layers.[64] Furthermore, as for carbon materials containing mainly basal planes, XPS analyses support the presence of numerous OFGs for such support. Since it is a carbon edge model, the experimentally detected abundant functionalities are located strictly in the zigzag termination,[14c] among which are ethers, isolated carbonyls, hydroxyls/phenolics, lactones, carboxylic, anhydrides, and carbene-like active sites (Figures S31e–q). All supports are modeled to have an even number of electrons, so an oxygen atom (as a carbonyl functional group on the opposite edge) is added to the systems incorporating carbene-like active sites, ethers, and isolated carbonyls.[65] For the other graphene nanoribbons, no additional heteroatom is needed. Importantly, the spin density distribution of these active sites showed significant electron spin polarization (spin density~1 electron spin).

Regarding the average structural information of the species present in Rh/CNF and Rh/FM, the main difference with respect to Rh/FLG and Rh/CNT is the exclusive presence of the first Rh–C shell (on both prismatic surfaces), the corresponding average bond lengths being around 2.08 and 2.07 Å for Rh/CNF and Rh/FM, respectively. Moreover, the Rh–C coordination in CNF and FM are comparable, leading to the deposition of similar metallic species. Given the lack of Rh–Rh distances (within the experimental sensitivity), these materials appear to mostly embed Rh_{SA} that are close to the edges of the carbon plane, with mean Rh–C coordination numbers between 4.7 (for Rh/FM) and 5.3 (for Rh/CNF). Unlike CNTs and FLG, for which the creation of surface defects plays a crucial role to stabilize Rh_{SA}, the presence of unsaturated carbon atoms at the edges of prismatic materials serves as anchoring sites for metal adsorption. Since the EXAFS characterization of Rh/CNF and Rh/FM shown a similar coordination environment for Rh_{SA}, the same catalyst models were developed for both. The energetic and structural characteristics and corresponding structures for the rhodium catalyst models are summarized in Table S12 and Figure S32, respectively. In general, the models turn out to be thermodynamically stable, with binding energies approaching 39 kcal mol^{-1}. Among H-terminated BZGNR, the asymmetric AC stacking (model CNF-5/FM-5) offers Rh–C structural parameters reasonably close to those found experimentally, although slightly overestimated (average bond length around 2.27 Å and mean CN of 6.00). However, modifying this stacking with O-containing functionalities leads to more competitive models, with bond lengths values dropping to 2.10 Å and mean CN of 5.00. These significant decreases allow for better EXAFS fitting. Consequently, the experimental data were fitted with these models and classified in terms of the usual goodness-of-fit values. Among the computational models for Rh/CNF that are consistent with the experimental data, we can find the supports with a carbene-like active site (model CNF-7), an ether oxygen atom (model CNF-9), or an isolated carbonyl motif (model CNF-11). For Rh/FM, the better models correspond to the supports with an isolated carbonyl (model FM-11), carboxyl (model FM-17) or hydroxyl motif stand out (model FM-13), considering the energetics and bonding distances along with the goodness of fit, the models were ranked and sorted out. From the coordination point of view, the only Rh_{SA} perfectly accommodated in the vicinity of the point defect occurs with the carbene-like active site because the zigzag edge continues to provide an unsaturated site (localized electronic state). The Rh_{SA} are pushed away from the OFGs due to saturation of the active carbons (non-magnetic local edge state), preferring to interact as in fully H-terminated edges. Consequently, the model presenting the greatest stability is the one decorated with the carbene-like active site, followed by those decorated with carboxyl, ether, carbonyl and hydroxyl, with binding energies of 23.7, 13.8, 5.1, 3.2 and 2.1 kcal mol^{-1}, respectively. Finally, considering exclusively the best model for Rh/CNF and Rh/FM (respectively carbene-like active site and isolated carbonyl motif), from the structure point of view they reproduce relatively well the EXAFS data, resulting in distances and reasonable average coordination numbers (2.18 Å and 5.00, respectively). The best models are shown in Figure 5h and Figure 5i, respectively, and Table 3, while the rest of the Rh/CNF models are represented in Figure S33 and Table S13, and for Rh/FM in Figure S34 and Table S14. The presence of a carbonyl near the Rh in the Rh/FM model may be correlated with the fact that XPS analyses showed that this catalyst contained more oxygen than Rh/CNF.

Finally, calculations were also performed to assess the effective atomic charges for the four best models shown on Figure 5. The results are presented on Table S15. The values obtained, $[Rh_{13}]^{3.2+}$ for Rh/FLG, $[Rh_2]^{1.6+}$ for Rh/CNT, and $[Rh_1]^{0.7+}$ for Rh/CNF and Rh/FM, agree with the pre-edge features of the XANES profiles of the four catalysts. These results also confirm the XPS analyses, which evidenced that the Rh species tend towards being cationic on all the carbon supports. It is worth noting that in the case of Rh/FLG, the loss of electron density from the Rh_{13} cluster to the support caused the charges in the upper and lower layers of the Rh_{13} cluster to be positive, $+0.6$ and $+2.6|e|$, respectively (Figure 5f). A different charge distribution was predicted for Rh_{13} on graphene oxide, a support showing a high concentration of OFGs.[41] In that case, the support induced an electronic redistribution of the Rh_{13}, the net charge being positive at the bottom region ($+1.6|e|$) but negative at the top ($-0.3|e|$). This should influence chemical reactivity.

Evaluation of Catalytic Performances

The results of the characterization of the four catalysts show that they present notable differences both in terms of support and active phase. The supports predominantly present different surfaces, decorated with different types and amounts of OFGs.

Rhodium species have different nuclearity (clusters and/or single atoms), are present on basal or prismatic surfaces and show various coordination. In particular, the analyses performed by XAS and XPS show the difficulty of detecting small quantities of clusters, which were visualized by STEM analyses in samples presenting essentially Rh_{SA}, such as the Rh/CNF catalyst (Figure S14). Recent studies have already highlighted this difficulty.[66] Other studies have shown that catalysis itself could constitute a powerful characterization tool for the study of this type of systems. Indeed, metallic species of various nuclearity[67] or metal single atoms of different coordination environment[68] show different reactivity. As reactions involving molecular hydrogen constitute the main industrial applications of carbon-supported precious metal catalysts,[69] the reactivity of the four catalysts have been investigated for different model reactions, including: the hydrogenation of phenylacetylene (PhA) and nitrobenzene (NB), and the hydroformylation of 1-octene (1-O) and styrene (ST). Each of these reactions, for which rhodium has been shown to be active, can provide important and complementary information on performance of the catalyst (activity, selectivity and stability), which is dependent on its structure. Indeed, catalyst performance can be impacted by each of the catalyst feature discussed below: nuclearity,[70] coordination,[71] and support surface chemistry.[72] Each of these catalytic reactions was repeated at least twice to ensure the reproducibility of the results obtained.

For hydrogenation reactions on noble metal catalysts, the significant energy barrier to achieving H_2 activation by heterolytic dissociation makes single atoms significantly less active than higher nuclearity species, for which facile homolytic H_2 dissociation may occur.[73] Recently, it was demonstrated that this disadvantage of single atoms in hydrogenation catalysis could be overcome by mixing them with nanoparticles or clusters on the same carbon support.[74] Molecular hydrogen is easily activated on metal nanoparticles/clusters, and hydrogen spillover provided M_{SA}–H species, which are more active than $M_{NP/cluster}$ for alkene/alkyne hydrogenation.[75]

Selective hydrogenation of PhA to ST is an important reaction to increase the purity of the styrene monomer. This reaction presents both conversion and selectivity issues. Although the hydrogenation of alkynes is usually performed under relatively mild conditions with Pd catalysts, both rhodium nanoparticles and single atoms have been reported to be active for this reaction.[76] In the case of Pd, it was shown that clusters or nanoparticles are much more active than single atoms,[77] and that Pd_{SA} can be more selective than $Pd_{NP/clusters}$.[75b] Cooperative catalysis between Pd nanoparticles/clusters and single atoms was also reported.[75b] The reaction was carried out at 100 °C and 5 bar of H_2 in methanol with a PhA/Rh molar ratio of 2000, and the results obtained are shown in Figure 6a. It is worth mentioning that contrarily to Pd catalysts, which allow running the reaction at room temperature, the use of rhodium requires higher temperature, since the reaction did not proceed at room temperature. This might be related to the lower ability of Rh to activate H_2. Indeed, although H_2 dissociative chemisorption is almost barrierless on Pd/C,[78] this is not the case for Rh/C.[79] The chemisorption of H_2 on the different model catalysts of Figure 5 was probed by DFT, confirming this statement. The estimated adsorption energies are -2.5 kcal mol^{-1} for Rh/CNF, -9.2 kcal mol^{-1} for Rh/FM, -16 kcal mol^{-1} for Rh/CNT and -17.5 kcal mol^{-1} for Rh/FLG. On the Rh_{13} cluster, the H–H bond is activated resulting in a bond-length of 1.01 Å. The catalyst activity (mol_{PhA} converted per mol of total Rh and per h) was measured after 2 hour reaction, and the selectivity of the catalyst toward ST was measured at 65% isoconversion. The catalyst with the highest proportion of metallic rhodium (Rh/FLG) is the most active, presenting a selectivity towards ST of 74%. In this catalyst, cooperative catalysis between $Rh_{clusters}$ and Rh_{SA} could be operative. The Rh/FM catalyst, which should present the highest proportion of Rh_{SA} (STEM, XPS and XAS analyses) is the least active but the most selective (S_{ST} 65% = 82%). HAADF-STEM analyses performed on this catalyst after the catalytic test confirm the stability of the Rh_{SA} under these conditions (Figure S35). The fact that Rh/CNT and Rh/CNF behave similarly in terms of activity (with an activity intermediate between Rh/FLG and Rh/FM) strongly suggests that the Rh/CNF sample must contain, as Rh/CNT, minimal amounts of Rh clusters that were not detected by XPS and XAS, but visualized by STEM (Figure S14). To evaluate the impact of Rh_{SA} location (basal versus prismatic plane) on catalyst performance, Rh/CNT and Rh/FM catalysts exhibiting a nominal Rh loading of 0.2% w/w (confirmed by ICP analyses) were independently prepared. These catalysts contain exclusively Rh_{SA} (Figure S36). Figure 7a and Figure S37 shows the performance of the two catalysts. The 0.2Rh/FM catalyst, for which Rh_{SA} are located on the prismatic surface is more active but less selective than the 0.2Rh/CNT catalyst, for which the Rh_{SA} are deposited on the basal surface. It is surprising that the 0.2Rh/FM catalyst is more active and less selective than the 1Rh/FM one (Figure S37). An explanation of this phenomenon could be an influence of the Rh_{SA} density on the catalytic performance. Recent developments of high-density SACs, which can be considered as representative of the 1Rh/FM catalyst, have shown that single-atom density affects the electronic structure and catalytic performance including for selective hydrogenation.[80]

However, there is no unified theoretical guidance to rationalize the site-site interaction in high-density SACs, and efforts are still needed to investigate such interactions for understanding structure-performance relationships. Since the Rh/FM catalyst shows the best performances in term of selectivity, we have examined its stability during six consecutives runs. The results of these experiences (Figure S38a) show the high stability of this catalyst during phenylacetylene hydrogenation. Finally, we also compared the performances of the Rh/FM catalyst with those of a commercial 5%Rh/C catalyst. Figure S38b shows the results obtained for a run of six hours with these two catalysts. The Rh/FM catalyst is more active and more selective than the Rh/C catalyst.

Hydrogenation of NB is an industrially important reaction leading to the production of aniline (AN) for the plastics industry. The use of this substrate is rationalized because, unlike PhA, NB contain a polar group, which upon coordination could favor the activation of H_2 on Rh_{SA}. Indeed, DFT calculations have

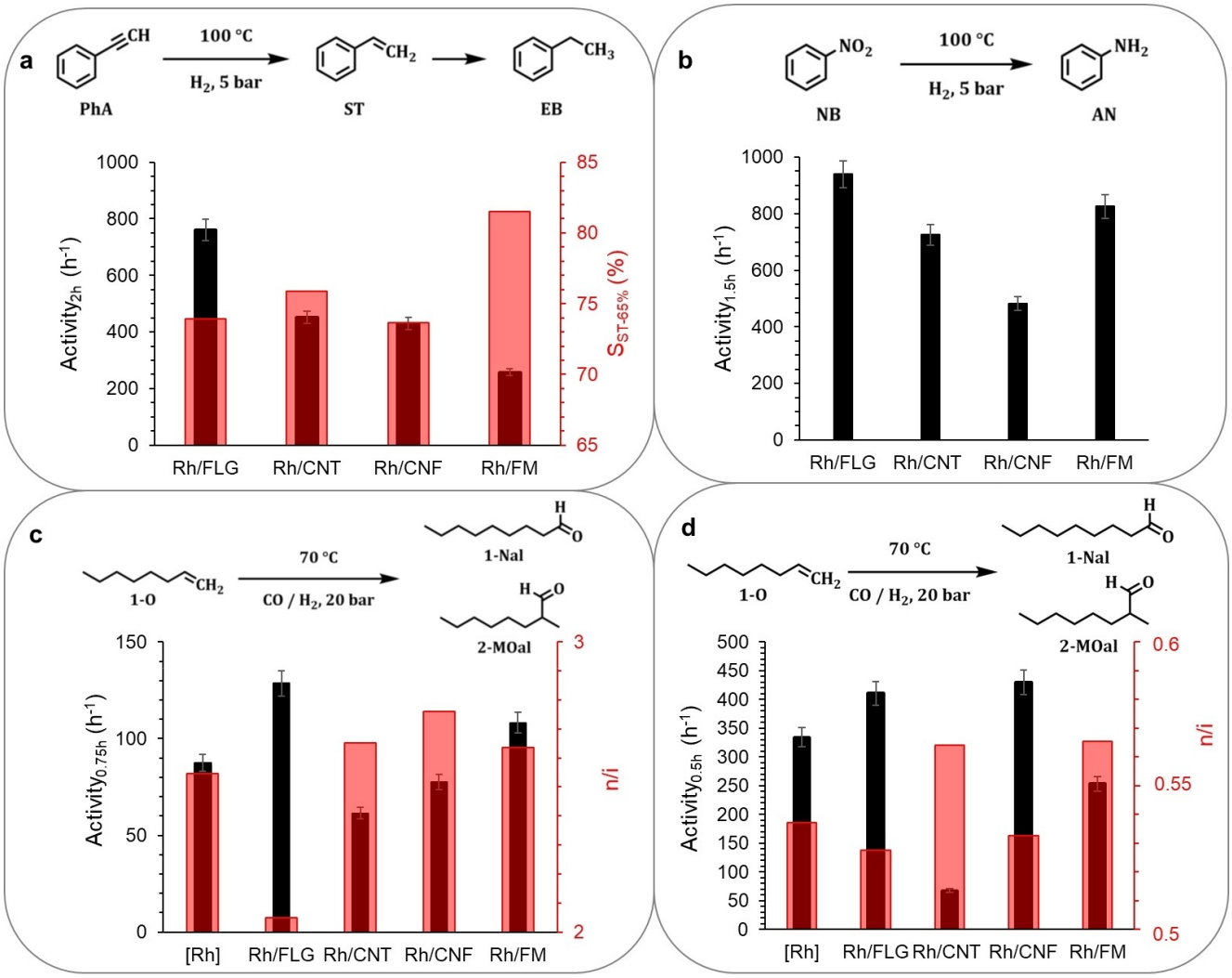

Figure 6. Catalytic results obtained with the four carbon-supported catalysts for: (a) phenylacetylene and (b) nitrobenzene hydrogenations; and (c) 1-octene and (d) styrene hydroformylations. Each experiment was repeated twice. The bars correspond to standard deviation.

shown that the co-adsorption of NB and H_2 could reduce the energetic barriers for the dissociation of H_2 on Rh_{SA}.[81] Highly dispersed Rh-based catalysts have been shown to be efficient and selective toward amino groups for the hydrogenation of nitroarene,[82] and cooperative catalysis between Rh_{SA} and Rh_{NP} has been reported.[82b] The hydrogenation of NB was carried out at 100 °C and 5 bar of H_2 in methanol with an NB/Rh molar ratio of 2500, and the results obtained are shown in Figure 6b. All catalysts produced selectively AN (Figure S39). The catalyst activity (mol_{NB} converted per mol of total Rh and per h) was measured after 1.5 hour reaction. As in the case of PhA hydrogenation, the most active catalyst is Rh/FLG, followed by Rh/CNT and Rh/CNF. This order of reactivity, Rh/FLG > Rh/CNT > Rh/CNF, should reflect the concentration of metallic Rh in these sample, which can perform the reaction directly or in synergy with Rh_{SA}.

The behavior of Rh/FM is significantly different in the hydrogenations of PhA and NB. Although this catalyst (at 1% w/w Rh) is the least active of the series in the hydrogenation of PhA, it performs almost as well as the Rh/FLG catalyst for NB hydrogenation. Since it has been shown that some carbon materials can catalyze this reaction with no metal addition,[83] the reactivity of the FM support was sought. After 1.5 h reaction with FM as catalyst, no conversion of NB was measured, precluding the direct involvement of the support to hydrogenate NB. The surface chemistry of the support can also impact the catalytic activity of the metal. Indeed, it was proposed that the presence of large amounts of OFGs on activated carbon supports positively influenced the adsorption of NB, which led to an improvement in hydrogenation rate.[84] Although these results could also arise from different porosity of the activated carbon supports,[85] we investigated the adsorption of NB on the four supports. Figure S40 shows that the FM support, which present the higher DFT surface area and amount of OFGs, adsorbed a twice as much NB as the other supports. This could contribute to the high activity of the Rh/FM catalyst.

Since DFT calculations have predicted that NB and H_2 co-adsorption could facilitated H_2 activation on Rh_{SA}, we also examined this by DFT for the four model catalysts. Interestingly

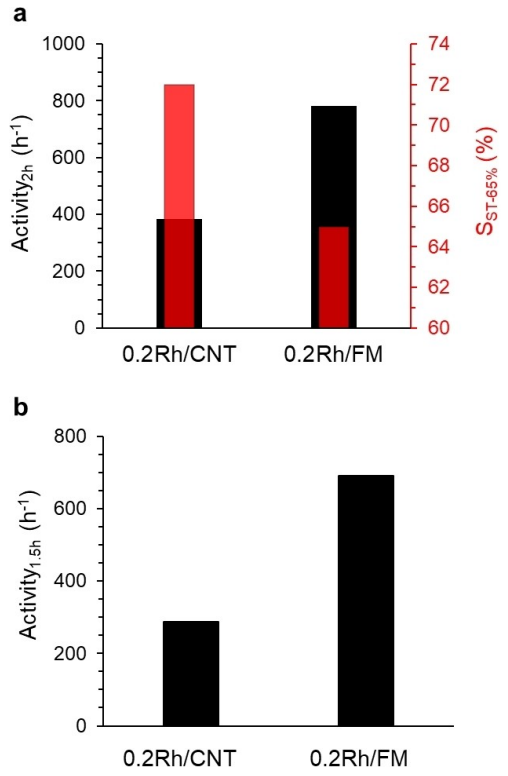

Figure 7. Catalytic results obtained with the Rh/CNT and Rh/FM catalysts for: (**a**) phenylacetylene; and (**b**) nitrobenzene hydrogenations.

for all the models, the NB adsorption is stronger than the one of H_2. The corresponding adsorption energies are -13.4 kcal mol^{-1} for Rh/FM, -19.6 kcal mol^{-1} for Rh/CNT, when it is -32.9 kcal mol^{-1} for Rh/CNF and -39.9 kcal mol^{-1} for Rh/FLG. Our attempts to coordinate both reactants on the proposed active site, show that: (i) for Rh/CNF configuration, H_2 is systematically repelled (Rh–H_2 distance is around 3.2 Å), (ii) co-adsorption is favorable for Rh/CNT system, (iii) this co-adsorption is also possible for Rh/FM and Rh/FLG, the latter being the most favorable due to the large number of available sites on the Rh cluster (see Figure S41 for optimized structures snapshots). In that specific case, the NB adsorption on the top site of the cluster even helps to dissociate H_2, the resulting H–H distance being 1.83 Å. Those statements can help to rationalize the catalytic properties of the different system. The weakest activity of the Rh/CNF systems may be related to the impossibility of co-adsorbing H_2 and NB directly, due to steric effect, meaning that the active site must be first hydrogenated. For the others three systems, activity is improved due to the presence in the vicinity of the active site of other species, such as metallic atoms (as in Rh/CNT or Rh/FLG) or O atoms, as in Rh/FM, that keeps H_2 molecules available for a further activation. As metal sintering was reported for Rh/C catalysts during NB hydrogenation,[86] we examined by AC HAADF-STEM the Rh/CNT and Rh/FM catalysts after catalysis. Figure S42 shows that significant sintering occurs for both catalysts. The presence of Rh nanoparticles on the FM support could also contribute to the high activity of this catalyst thanks to cooperative catalysis between Rh_{SA} and nanoparticles.

For this reaction also, the impact of Rh_{SA} location (basal versus prismatic plane) on catalyst performance was evaluated with the 0.2%Rh/CNT and 0.2%Rh/FM catalysts (Figure 7b). As for PhA hydrogenation, the activity measured for the 0.2%Rh/FM catalyst is more than double than that measured for 0.2% Rh/CNT, confirming the higher activity of Rh_{SA} deposited on the prismatic surface. However, since in that case metal sintering occurs, we cannot preclude a cooperative catalysis between Rh_{SA} and $Rh_{clusters}$ that will be more efficient on the 0.2%Rh/FM catalyst. Indeed, this support, which contain higher amount of OFGs, should allow an enhanced H-spillover.[53]

Hydroformylation is a process for the production of aldehydes from alkenes and syngas, which is conducted industrially with homogeneous Rh or Co catalysts.[87] Significant efforts have been devoted to developing supported Rh catalysts containing nanoparticles, clusters or even single atoms for this reaction.[88] As for hydrogenation reactions, cooperativity between Rh_{SA} and $Rh_{clusters}$ was reported for the hydroformylation reaction.[89] Recurring problems related to the use of such systems are: (i) the release of rhodium in solution (leaching) under hydroformylation conditions,[90] and (ii) selectivity issues for aliphatic substrates due to the high isomerization/hydrogenation rate of such alkenes.[72,91] The study of this reaction should allow obtaining information on the influence of the Rh environment on the stability of the catalyst against leaching, as well as on the selectivity obtained. Selectivity refers to side reactions such as isomerization (chemoselectivity), but the most important is regioselectivity, since both linear (*n*) and branched (*iso*) aldehydes can be produced from terminal olefins. The hydroformylation of 1-O was carried out at 70 °C and 20 bar ($CO/H_2 = 1$) in toluene with a 1-O/Rh molar ratio of 1000. The performances of the four supported catalysts were compared with a homogeneous catalyst, the rhodium(I) [$Rh(CO)_2(acac)$] complex, abbreviated as [Rh]. The catalyst activity ($mol_{1\text{-}O}$ converted per mol of total Rh and per h) was measured in a 0.75 hour reaction and the results obtained are shown in Figure S43a. Isomerization of the 1-O double bond occurred largely during the reaction, regardless of the catalytic system used (Figure S43b). The aldehydes, 1-nonanal (1-Nal) and 2-methyloctanal (2-MOal), were obtained together with large amounts (>90%) of isomerization products (no hydrogenation to octane was observed). This significant isomerization may be related to the conditions used (relatively low pressure and temperature), which are known to favor isomerization over hydroformylation.[92] Significant Rh leaching for the supported catalysts was measured by ICP analyses performed on the post-test solutions after catalyst filtration (Figure S43a). As expected, the most important leaching was measured for Rh/FLG, *i.e.*, the catalyst showing the highest proportion of metallic Rh, since for the metal SA to be stable, its binding energy to the support must be greater than the cohesion energy of the bulk metal.[93] The Rh/CNT catalyst, which presents a higher proportion of metallic Rh than Rh/CNF and Rh/FM, shows the lowest leaching value of the series, indicating that, under these conditions, the Rh_{SA} coordination on the basal/defect surface (Rh/CNT) is more

stabilizing than on the prismatic surface (Rh/CNF and Rh/FM). This agrees with the XAS measurements, which give a shorter Rh–C bond length in the Rh/CNT sample (1.90 Å, CN = 4.2) than in Rh/CNF (2.02 Å, CN = 5.3) and Rh/FM (2.06 Å, CN = 4.7). The measured leaching values suggest that part of the activity of the supported catalysts is linked to molecular species in solution. However, the measured activities remain high enough to be able to state that Rh_{SA} must contribute significantly to the activity (Figure S43c). It should be noted that although the Rh/CNF and Rh/FM catalysts have similar leaching values (~35%), their activities are significantly different, with the Rh/FM catalyst being even more active than the molecular complex. Considering the fact that Rh/CNF and Rh/FM catalysts present a similar surface concentration of Rh (XPS) and a similar environment for Rh_{SA} (XAS), this difference in reactivity suggests that, as in homogeneous catalysis, subtle changes in the coordination sphere of the Rh_{SA} (Figures 5g–h) can significantly impact catalytic performance. The performance of the series of catalyst related to hydroformylation (aldehyde production) is reported in Figure 6c. The hydroformylation activity follows the same trend as the overall activity (Figure S44). The n/i ratio (linear to branched aldehydes) ranged between 2.5–2.8 for all catalysts, except for Rh/FLG, which presents a ratio slightly lower than 2. Although reasons related to the steric hindrance (long or short range) to explain differences in regioselectivity have been proposed,[94] electronic effects have also been advanced.[95] Difference of n/i ratio during hydroformylation of hexene on Rh/C catalysts prepared on different carbon supports have already been reported.[96] In particular, significant drops of the n/i ratio were observed when the alkene conversion approached 100%. The notable decrease of the n/i ratio was attributed to the hydroformylation of internal alkenes. In our case, the conversion achieved with the Rh/FLG catalyst is 98% in 30 minutes, while it ranges between 50–80% for the other catalysts (Figure S43b). The lower n/i ratio obtained with the Rh/FLG catalyst was therefore attributed to the hydroformylation of the internal octenes on this catalyst, which is the most active.

The same series of catalysts was tested for the hydroformylation of ST. In that case, no chemoselectivity issues are expected, explaining why the performance of SACs are usually evaluated on this substrate. The hydroformylation of ST was carried out at 100 °C and 20 bar ($CO/H_2 = 1$) in toluene with a ST/Rh molar ratio of 1000 and the performance of the catalyst series is reported in Figure 6d. The catalyst activity (mol_{ST} converted per mol of total Rh and per h) was measured after 1.5 hour reaction. Significant leaching of Rh was also measured, between 50–60% for Rh/FLG, Rh/CNF and Rh/FM, and only 24% for Rh/CNT, confirming the higher stability of Rh_{SA} in this catalyst. We observed by AC HAADF-STEM the Rh/FM catalyst after an hydroformylation test to probe the nuclearity of Rh species. Figure S45 shows that the remaining rhodium is mainly present as single atoms on the used catalyst, and no significant aggregation was observed, indicating the robust nature of some Rh_{SA}. As for O-1 hydroformylation, the Rh/FLG catalyst is more active than the molecular catalyst and Rh/CNT presents the lowest activity. Keeping the balance between stability (Rh/CNT) and activity (Rh/FLG) is therefore a challenge, as reported for oxide supported Rh_{SA} hydroformylation catalysts.[91,97] Surprisingly, the order of reactivity of Rh/CNF and Rh/FM is inverse compared to O-1 hydroformylation, with Rh/CNF being the most active catalyst. The n/i ratio does not change much between the different catalysts. However, leaching of metal species in solution, resulting in potential contributions from homogeneously catalyzed pathways and net metal losses, often remains a major concern.

This study on the catalytic reactivity of the produced catalysts confirms the importance that such characterization can have, which is an essential complement to spectroscopic and microscopy studies. In particular, the study of reactivity makes it possible to refine the characterization in terms of speciation, a parameter often neglected in studies aiming to compare the reactivity of SACs to those of clusters or nanoparticles. Indeed, there is still a lack of analytical techniques that can readily provide quantitative information on the atomic fractions of metal single atoms and the co-existence of metallic clusters.[98]

Conclusions

A series of supported catalysts containing Rh single atoms has been prepared on carbon materials presenting different basal/prismatic surfaces. The structural characterization coupled to modeling suggests a higher proportion of metal single atoms on carbon materials presenting prismatic surface. Unlike materials presenting basal surfaces, for which the creation of surface defects plays a key role to stabilize single atoms, the presence of unsaturated carbon atoms at the edges of prismatic surface serves as efficient anchoring sites for metal adsorption. Overall, our results confirm the difficulty in detecting few amounts of small clusters in samples containing predominantly supported metal single atoms, even combining several cutting-edge analysis techniques.[64] The study of the chemical reactivity of such systems proves to be a valuable tool for detailed characterization due to the significant differences in reactivity and in stability, which can be linked to the speciation of the species present and to their chemical environment. The study of the chemical environment of metal single atoms by DFT-guided XAS in the case of supports that may present different anchoring sites is also delicate, since this approach is predominantly model-dependent and do not consider the presence of mixtures. New machine learning-based tools must be developed for more detailed analysis of such systems.[57c,99] Such an approach should allow the development of efficient catalysts integrating an ultra-rational use of often expensive and scarce metals.

Materials and Methods

Carbon Material Synthesis

The carbon nanotubes were produces by catalytic-CVD in a fluidized bed reactor using ethylene as carbon source. An $AlFeCoO_4$ catalyst was first pre-reduced under hydrogen during 30 min at 650 °C. A typical experiment was carried out with ethylene (600 mL min^{-1}) for 30 min at 675 °C. The produced CNTs were purified (catalyst dissolution) by an aqueous solution of H_2SO_4 (50 vol%, 95% AnalaR NORMAPUR analytical reagent) under reflux for 3 h. The fibrous material (FM) was prepared using the same procedure, but in that case a $CuNiCoO_4$ catalyst was used. The carbon nanofibers and few layer graphene are two commercial products. The CNFs were purchased from GANF (Grupo Antolin Nano Fibras), and the FLG was purchased from Avanzare (avanPLAT-7) and no further purification was done for these two commercial materials. The materials were functionalized by a treatment with HNO_3 (VWR, nitric acid 65% AnalaR NORMAPUR) under reflux at 140 °C for 3 h. The mixture was then filtered and washed with distilled water until neutral pH was obtained. The finals products were then dried at 80 °C overnight.

Rh Catalyst Synthesis

A dry impregnation method was used to prepare the carbon-supported rhodium catalysts. The carbon materials were first activated in a horizontal tubular oven under Ar (210 mL min^{-1}) at 400 °C. Then, the desired amount of rhodium (III) triallyl ([$Rh(allyl)_3$]) was added to pentane (30 mL, VWR, 99%, HiPerSolv CHROMANORM for HPLC) containing 1 g of activated carbon material to introduce 1% w/w of the metallic phase. The solution was then stirred for 1 h, washed 3 times with pentane and finally dried under vacuum overnight; the whole process is done under an inert atmosphere. At last, the catalysts were reduced at 80 °C under H_2 (60 mL min^{-1}) and Ar (245 mL min^{-1}) for 1 h.

Material Characterization

The metal content in the catalytic materials was measured by inductively coupled plasma optical emission spectroscopy (ICP-OES) performed on a Thermo Scientific ICAP 6300 instrument.

TEM analyses were performed by using a JEOL JEM 1400 electron microscope operating at 120 kV. The high-resolution analyses were conducted by using a JEOL JEM 2100 f microscope equipped with a field emission gun (FEG) operating at 200 kV with a point resolution of 2.3 Angstrom and a JEOL JEM-ARM200F Cold FEG operating at 200 kV with a point resolution of > 1.9 Angstrom. The particle size distribution was determined through a manual measurement of enlarged micrographs from different areas of the TEM grid (at least 300 particles).

X-ray powder diffraction patterns were obtained at room temperature with a MiniFLex600 diffractometer, employing Cu Kα radiation (λ = 1.54187 Å).

Raman spectra were obtained on a micro-Raman setup (Una labram HR800 Jobin Yvon spectrometer). A laser of 532 nm wavelength was used as excitation source with a maximum power of 7 mW.

Nitrogen adsorption measurements were performed at −196 °C using a 3Flex Surface Characterization Analyzer (Micromeritics GmbH). Before analysis, the samples were degassed at 150 °C using a Micromeritics VacPrep 061 Sample Degas System until a static pressure of less than 0.01 Torr (0.0133 mbar) was reached. The adsorptive potential distributions were calculated from the adsorption isotherms using the standard instrument software (3Flex Version 4.04). The calculation of the DFT, basal plane and "non-basal plane" surfaces as well as of the respective ratios has been performed as described in the literature.[100]

HT-TPD was conducted using an in-house system following the pre-established method.[30a] For calculating the number of edge sites we took into account the amounts of hydrogen. Note that the number of H-terminated edge sites (NH-terminated) was calculated by doubling the amount of H_2 gas measured since one molecule of H_2 is produced from two H-terminated edge sites. Using the number of edge sites, the surface area of the edge sites, S_{edge}, can be further calculated.[30a] Using the area assigned to each carbon atom from:

$$S_{edge} = N_{edge} \times A_{edge} \times N_A$$

Where $A_{edge} = 0.083\ nm^2$ is the calculated average area of each carbon atom and $N_A = 6.022 \times 10^{23}\ mol^{-1}$.

XPS spectra were recorded in a Thermo Electron Ka spectrometer using with a Al Ka (1487.7 eV) X-ray source and a dual beam (e^- and Ar^+) charge neutralization. For these spectra, we used a 20 eV pass energy, a 0.1 eV energy step and a dwell time of 250 ms. CasaXPS® was used for data treatment.

X-ray absorption spectra at Rh K-edge were taken at the 8-ID(SS) beamline of NSLS-II at Brookhaven National Laboratory. An Si(111) double crystal monochromator was used. The Rh deposited on different carbon supports were measured in fluorescence mode. The raw XAFS spectra were analyzed utilizing the Athena and Artemis interfaces of the Demeter software package.[101] The k^2-weighted EXAFS oscillation in the range 3–14 Å was Fourier-transformed and curve-fitting analysis was performed in the range 0–5 Å in R space. The amplitude reduction factor was estimated by fitting the spectrum of Rh foil with the parameters calculated with FEFF-6.[102] The curve-fitting analysis was performed considering the crystal structures of the models developed from DFT.

Computational Details

Periodic DFT calculations were performed using the *ab initio* plane-wave pseudopotential approach as implemented in the Vienna Ab initio Simulation Package (VASP 5.4).[103] The Perdew – Burke – Ernzerhof exchange – correlation functional within the spin-polar-

ized generalized gradient approximation was chosen,[104] and van der Waals interactions were taken into account through the D3 method of Grimme *et al.* with zero-damping function.[105] The innermost electrons were replaced by a projector-augmented wave (PAW) approach,[106] while the valence monoelectronic states were expanded in a plane-wave basis set with a cut-off energy of 500 eV. Partial occupancies were estimated with a Gaussian smearing (σ) of 0.05 eV during all relaxations and extrapolating the energies to σ = 0.00 eV. Basal (carbon nanotubes, CNT, and few-layer graphene, FLG) and prismatic (fibrous materials, FM, and carbon nanofibers, CNF) model carbon supports consist respectively of a three-layer rhombohedral graphene slab with ABC stacking order, and of a two-layer zigzag graphene nanoribbon slab with hydrogen-terminated z_1 configuration (dangling bonds saturated with a single hydrogen per carbon atom). Both systems, containing 98 °C atoms per layer in a *p*(7×7) supercell, were modeled large enough to include a broad representation of the experimentally observed surface oxygen functionalities and correctly describe the magnetic edge states in the prismatic plane. Γ-centered 3×3×1 and 3×1×1 *k*-point grids generated using the Monkhorst-Pack method were employed as a good compromise between accuracy and computational cost for the basal and prismatic slab models, respectively.[107] Spurious interactions between the modelled slab and its perpendicular periodic images were eliminated by adding a vacuum region by at least 15 Å, and by considering a dipole correction to the total energy along the *z*-direction.[108] Iterative relaxation of atomic positions proceeded until the change in total energy between successive steps was less than 10^{-5} eV and the residual forces on any direction acting on the atoms were less than 0.02 eV $Å^{-1}$.

Catalytic Experiments

Hydrogenation reactions were performed in a Top Industrie high pressure and temperature stainless-steel autoclave equipped with an anti-vortex device and a T,P controlling system.

Hydrogenation of Phenylacetylene

In a typical experiment, a mixture containing the Rh catalyst, 40 mL of a phenylacetylene (Aldrich, 98%) solution in methanol (VWR, methanol HiPerSolv Chromanorm for HPLC, isocratic grade, PhA/Rh = 2000, 2 mmol of PhA) and decane (75 mg, internal standard) was transferred into the autoclave. The autoclave was purged by three vacuum/H_2 cycles, heated at 100 °C and pressurized at 5 bars of H_2; the stirring rate was fixed at 700 rpm to avoid mass transfer limitations. The reaction was followed for 6 hours taking a sample every hour. Samples of the reaction mixture were analyzed by GC.

Hydrogenation of Nitrobenzene

In a typical experiment, a mixture containing the Rh catalyst, 40 mL of a nitrobenzene (Millipore) solution in methanol (VWR, methanol HiPerSolv Chromanorm for HPLC, isocratic grade, PhA/Rh = 2500, 2.5 mmol of NB) and decane (75 mg, internal standard) was transferred into the autoclave. The autoclave was purged by three vacuum/H_2 cycles, heated at 100 °C and pressurized at 5 bars of H_2; the stirring rate was fixed at 700 rpm to avoid mass transfer limitations. The reaction was followed for 2 hours taking a sample every 30 minutes. Samples of the reaction mixture were analyzed by GC.

Hydroformylation of 1-Octene

In a typical experiment, a mixture containing the Rh catalyst, 20 mL of a 1-octene (Acros Organics) solution in toluene (VWR toluene HiPerSolv chromanorm for HPLC, 1-O/Rh = 1000, 1 mmol of 1-O) and decane (75 mg, internal standard) was transferred into the autoclave. The autoclave was purged by three vacuum/CO + H_2 cycles, heated at 70 °C and pressurized at 20 bars of CO + H_2 (1/1); the stirring rate was fixed at 1000 rpm to avoid mass transfer limitations. The reaction mixture was analyzed after 45 min by GC.

Hydroformylation of Styrene

In a typical experiment, a mixture containing the Rh catalyst, 30 mL of a styrene (Aldrich) solution in toluene (VWR toluene HiPerSolv chromanorm for HPLC, ST/Rh = 1000, 1.5 mmol of ST) and decane (75 mg, internal standard) was transferred into the autoclave. The autoclave was purged by three vacuum/CO + H_2 cycles, heated at 70 °C and pressurized at 20 bars of CO + H_2 (1/1); the stirring rate was fixed at 1000 rpm to avoid mass transfer limitations. The reaction was followed for 3 hours taking a sample every 30 minutes. Samples of the reaction mixture were analyzed by GC.

Adsorption of Nitrobenzene

Adsorption tests were performed in glass flasks. In a typical experiment, a solution of 0.005 M of nitrobenzene was prepared with decane as a standard in methanol. This initial solution concentration was measured by GC. Some of this solution (5 mL) was added to a flask with some catalyst (150 mg). The flask was sealed to avoid any evaporation of the solvent and stirred at 500 rpm for an hour. The solution was then filtered and analyzed again by GC to determine the amount of nitrobenzene adsorbed on the catalysts.

Author Contributions

The manuscript was written through contributions of all authors. All authors have given approval to the final version of the manuscript.

Acknowledgements

This work has received funding from the French Agence Nationale de la Recherche under grant agreement ANR-19-CE07-0030 (COMET) and ANR-21-CE07-0021 (GRAAL). This work was also supported by ECOS Sud - ANID (project ECOS n° C21E03). J.N.-R., I.d.R., and I.C.G. thankfully acknowledge the computer resources through the "Calcul en Midi-Pyrénées" initiative CALMIP (projects p0812 and p1214), and CINES, IDRIS, and TGCC under the allocation 2022-A0120906649 made by GENCI. A.I.F. acknowledges support of the U. S. DOE, Office of Science, Office of Basic Energy Sciences grant no. DE-SC0022199. J.P. and V. P. acknowledge Cooperative Agreement W56HZV-19-2-0001 U.S. Army DEVCOM Ground Vehicle Systems Center (GVSC) and University of Michigan Automotive Research Centre Fund (SUBK00019353).

Conflict of Interests

The authors declare no conflict of interest.

Data Availability Statement

The data that support the findings of this study are available from the corresponding author upon reasonable request.

Keywords: Single atom catalysis · Carbon materials · Rhodium · Hydrogenation · Hydroformylation

[1] D. Pham Minh, P. Serp in *Supported Metal Single Atom Catalysis*, (Eds.: P. Serp, D. Pham Minh), Wiley, Weinheim **2022**, 1–49.
[2] Q. Zhang, J. Guan, *Nano Res.* **2022**, *15*, 38–70.
[3] a) W. Liu, Y. Chen, H. Qi, L. Zhang, W. Yan, X. Liu, X. Yang, S. Miao, W. Wang, C. Liu, A. Wang, J. Li, T. Zhang, *Angew. Chem. Int. Ed.* **2018**, *57*, 7071–7075; b) K. Liu, X. Zhao, G. Ren, T. Yang, Y. Ren, A. F. Lee, Y. Su, X. Pan, J. Zhang, Z. Chen, J. Yang, X. Liu, T. Zhou, W. Xi, J. Luo, C. Zeng, H. Matsumoto, W. Liu, Q. Jiang, K. Wilson, A. Wang, B. Qiao, W. Li, T. Zhang, *Nat. Commun.* **2020**, *11*, 1263; c) H. Qi, J. Yang, F. Liu, L. Zhang, J. Yang, X. Liu, L. Li, Y. Su, Y. Liu, R. Hao, A. Wang, T. Zhang, *Nat. Commun.* **2021**, *12*, 3295.
[4] G. Malta, S. A. Kondrat, S. J. Freakley, C. J. Davies, L. Lu, S. Dawson, A. Thetford, E. K. Gibson, D. J. Morgan, W. Jones, P. P. Wells, P. Johnston, C. R. A. Catlow, C. J. Kiely, G. J. Hutchings, *Science* **2017**, *355*, 1399–1403.
[5] Y. Zhang, J. Yang, R. Ge, J. Zhang, J. M. Cairney, Y. Li, M. Zhu, S. Li, W. Li, *Coord. Chem. Rev.* **2022**, *461*, 214493.
[6] M. Kottwitz, Y. Li, H. Wang, A. I. Frenkel, R. G. Nuzzo, *Chemistry-Methods* **2021**, *1*, 278–294.
[7] K. Qi, M. Chhowalla, D. Voiry, *Mater. Today* **2020**, *40*, 173–192.
[8] C. Rivera-Cárcamo, P. Serp, *ChemCatChem* **2018**, *10*, 5058–5091.
[9] M. B. Gawande, P. Fornasiero, R. Zbořil, *ACS Catal.* **2020**, *10*, 2231–2259.
[10] a) P. Serp(Eds: J., Reedijk, K., Poeppelmeier) Elsevier, Amsterdam **2013** in *Comprehensive Inorganic Chemistry II (Second Edition)* 323–369; b) Y. Ding, Z.-A. Qiao, *Adv. Mater.* **2022**, *34*, 2206025.
[11] a) I. C. Gerber, P. Serp, *Chem. Rev.* **2020**, *120*, 1250–1349; b) H.-Y. Zhuo, X. Zhang, J.-X. Liang, Q. Yu, H. Xiao, J. Li, *Chem. Rev.* **2020**, *120*, 12315–12341.
[12] C. F. Sanz-Navarro, P.-O. Åstrand, D. Chen, M. Rønning, A. C. T. van Duin, T. Jacob, W. A. Goddard, *J. Phys. Chem. A* **2008**, *112*, 1392–1402.
[13] X. Fu, X. Zhao, T.-B. Lu, M. Yuan, M. Wang, *Angew. Chem. Int. Ed.* **2023**, *62*, e202219242.
[14] a) T. J. Bandosz (Eds: P., Serp, J. L., Figueiredo) Wiley, Hoboken **2008** in *Carbon Materials for Catalysis* 45–92; b) A. Rehman, M. Park, S.-J. Park, *Coatings* **2019**, *9*, 103; c) J. Zhou, P. Yang, P. A. Kots, M. Cohen, Y. Chen, C. M. Quinn, M. D. de Mello, J. Anibal Boscoboinik, W. J. Shaw, S. Caratzoulas, W. Zheng, D. G. Vlachos, *Nat. Commun.* **2023**, *14*, 2293.
[15] F. Herold, J. Gläsel, B. J. M. Etzold, M. Rønning, *Chem. Mater.* **2022**, *34*, 8490–8516.
[16] a) B. F. Machado, M. Oubenali, M. Rosa Axet, T. Trang Nguyen, M. Tunckol, M. Girleanu, O. Ersen, I. C. Gerber, P. Serp, *J. Catal.* **2014**, *309*, 185–198; b) H. Jiang, L. Zhu, K.-s. Moon, C. P. Wong, *Carbon* **2007**, *45*, 655–661.
[17] a) D. Y. Kim, D. S. Jeong, P. Thangavel, M. Ha, H. Hwang, Y.-J. Park, T. J. Shin, D.-H. Seo, H. S. Shin, K. S. Kim, *Chem* **2023**; b) M. Mahmoodinia, P.-O. Åstrand, D. Chen, *J. Phys. Chem. C* **2017**, *121*, 20802–20812.
[18] Y. Zhang, J. Zhang, D. S. Su, *ChemSusChem* **2014**, *7*, 1240–1250.
[19] M. Inagaki, M. Toyoda, Y. Soneda, T. Morishita, *Carbon* **2018**, *132*, 104–140.
[20] a) Z. Shi, W. Yang, Y. Gu, T. Liao, Z. Sun, *Adv. Sci.* **2020**, *7*, 2001069; b) H. Nishihara, T. Hirota, K. Matsuura, M. Ohwada, N. Hoshino, T. Akutagawa, T. Higuchi, H. Jinnai, Y. Koseki, H. Kasai, Y. Matsuo, J. Maruyama, Y. Hayasaka, H. Konaka, Y. Yamada, S. Yamaguchi, K. Kamiya, T. Kamimura, H. Nobukuni, F. Tani, *Nat. Commun.* **2017**, *8*, 109.
[21] J. Zhu, P. Xiao, H. Li, S. A. C. Carabineiro, *ACS Appl. Mater. Interf.* **2014**, *6*, 16449–16465.
[22] Z. Chen, E. Vorobyeva, S. Mitchell, E. Fako, N. López, S. M. Collins, R. K. Leary, P. A. Midgley, R. Hauert, J. Pérez-Ramírez, *Natl. Sci. Rev.* **2018**, *5*, 642–652.
[23] a) M. E. Vol'pin, Y. N. Novikov, N. D. Lapkina, V. I. Kasatochkin, Y. T. Struchkov, M. E. Kazakov, R. A. Stukan, V. A. Povitskij, Y. S. Karimov, A. V. Zvarikina, *J. Am. Chem. Soc.* **1975**, *97*, 3366–3373; b) A. T. Shuvayev, B. Y. Helmer, T. Lyubeznova, V. L. Kraizman, A. S. Mirmilstein, L. D. Kvacheva, Y. N. Novikov, M. E. Volpin, *J. Phys. France* **1989**, *50*, 1145–1151.
[24] U. Petek, F. Ruiz-Zepeda, M. Bele, M. Gaberšček, *Catalysts* **2019**, *9*, 134.
[25] a) H. Yan, X. Zhao, N. Guo, Z. Lyu, Y. Du, S. Xi, R. Guo, C. Chen, Z. Chen, W. Liu, C. Yao, J. Li, S. J. Pennycook, W. Chen, C. Su, C. Zhang, J. Lu, *Nat. Commun.* **2018**, *9*, 3197; b) C. Tsounis, B. Subhash, P. V. Kumar, N. M. Bedford, Y. Zhao, J. Shenoy, Z. Ma, D. Zhang, C. Y. Toe, S. Cheong, R. D. Tilley, X. Lu, L. Dai, Z. Han, R. Amal, *Adv. Funct. Mater.* **2022**, *32*, 2203067; c) B.-W. Zhang, T. Zheng, Y.-X. Wang, Y. Du, S.-Q. Chu, Z. Xia, R. Amal, S.-X. Dou, L. Dai, *Commun. Chem.* **2022**, *5*, 43; d) H. Yan, H. Cheng, H. Yi, Y. Lin, T. Yao, C. Wang, J. Li, S. Wei, J. Lu, *J. Am. Chem. Soc.* **2015**, *137*, 10484–10487; e) F. Huang, Y. Deng, Y. Chen, X. Cai, M. Peng, Z. Jia, P. Ren, D. Xiao, X. Wen, N. Wang, H. Liu, D. Ma, *J. Am. Chem. Soc.* **2018**, *140*, 13142–13146; f) Q. Yang, H. Liu, P. Yuan, Y. Jia, L. Zhuang, H. Zhang, X. Yan, G. Liu, Y. Zhao, J. Liu, S. Wei, L. Song, Q. Wu, B. Ge, L. Zhang, K. Wang, X. Wang, C.-R. Chang, X. Yao, *J. Am. Chem. Soc.* **2022**, *144*, 2171–2178; g) H. Wei, K. Huang, D. Wang, R. Zhang, B. Ge, J. Ma, B. Wen, S. Zhang, Q. Li, M. Lei, C. Zhang, J. Irawan, L.-M. Liu, H. Wu, *Nat. Commun.* **2017**, *8*, 1490; h) D. Liu, X. Li, S. Chen, H. Yan, C. Wang, C. Wu, Y. A. Haleem, S. Duan, J. Lu, B. Ge, P. M. Ajayan, Y. Luo, J. Jiang, L. Song, *Nat. Energy* **2019**, *4*, 512–518; i) L. Zhang, Y. Jia, G. Gao, X. Yan, N. Chen, J. Chen, M. T. Soo, B. Wood, D. Yang, A. Du, X. Yao, *Chem* **2018**, *4*, 285–297; j) X. Huang, H. Yan, L. Huang, X. Zhang, Y. Lin, J. Li, Y. Xia, Y. Ma, Z. Sun, S. Wei, J. Lu, *J. Phys. Chem. C* **2019**, *123*, 7922–7930; k) H. Cheng, I. Kvande, Y.-A. Zhu, N. Hammer, M. Rønning, J. C. Walmsley, P. Li, Z. Qi, X.-G. Zhou, D. Chen, *J. Phys. Chem. C* **2018**, *122*, 7166–7178; l) R. E. Ambrusi, C. R. Luna, M. G. Sandoval, P. Bechthold, M. E. Pronsato, A. Juan, *Appl. Surf. Sci.* **2017**, *425*, 823–832.
[26] Z. Fang, L. Li, D. A. Dixon, R. R. Fushimi, E. J. Dufek, *J. Phys. Chem. C* **2021**, *125*, 20686–20696.
[27] a) J. Zhu, A. Holmen, D. Chen, *ChemCatChem* **2013**, *5*, 378–401; b) K. Zaghib, G. Nadeau, K. Kinoshita, *J. Power Sources* **2001**, *97–98*, 97–103.
[28] a) J. P. Olivier, M. Winter, *J. Power Sources* **2001**, *97–98*, 151–155; b) T. Placke, V. Siozios, R. Schmitz, S. F. Lux, P. Bieker, C. Colle, H. W. Meyer, S. Passerini, M. Winter, *J. Power Sources* **2012**, *200*, 83–91; c) Z. Li, H. Peng, R. Liu, Y. Mo, B. Cao, W. Lai, X. Li, L. Pan, Y. Chen, *J. Power Sources* **2020**, *457*, 228022.
[29] V. Meunier, C. Ania, A. Bianco, Y. Chen, G. B. Choi, Y. A. Kim, N. Koratkar, C. Liu, J. M. D. Tascon, M. Terrones, *Carbon* **2022**, *195*, 272–291.
[30] a) T. Ishii, S. Kashihara, Y. Hoshikawa, J.-i. Ozaki, N. Kannari, K. Takai, T. Enoki, T. Kyotani, *Carbon* **2014**, *80*, 135–145; b) K. Wakabayashi, T. Yoshii, H. Nishihara, *Carbon* **2023**, *210*, 118069.
[31] I. Gerber, M. Oubenali, R. Bacsa, J. Durand, A. Gonçalves, M. F. R. Pereira, F. Jolibois, L. Perrin, R. Poteau, P. Serp, *Chem. Eur. J.* **2011**, *17*, 11467–11477.
[32] M. Smith, L. Scudiero, J. Espinal, J.-S. McEwen, M. Garcia-Perez, *Carbon* **2016**, *110*, 155–171.
[33] P. M. A. Sherwood, *J. Electron Spectrosc. Relat. Phenom.* **1996**, *81*, 319–342.
[34] Y.-Q. Wang, H. Viswanathan, A. A. Audi, P. M. A. Sherwood, *Chem. Mater.* **2000**, *12*, 1100–1107.
[35] Y. Xie, P. M. A. Sherwood, *Chem. Mater.* **1991**, *3*, 164–168.
[36] C. Rivera-Cárcamo, C. Scarfiello, A. B. García, Y. Tison, H. Martinez, W. Baaziz, O. Ersen, C. Le Berre, P. Serp, *Adv. Mater. Interfaces* **2021**, *8*, 2001777.
[37] N. Wang, Q. Sun, T. Zhang, A. Mayoral, L. Li, X. Zhou, J. Xu, P. Zhang, J. Yu, *J. Am. Chem. Soc.* **2021**, *143*, 6905–6914.
[38] C.-T. Kuo, Y. Lu, L. Kovarik, M. Engelhard, A. M. Karim, *ACS Catal.* **2019**, *9*, 11030–11041.
[39] a) S. M. Choi, M. H. Seo, H. J. Kim, W. B. Kim, *Synth. Met.* **2011**, *161*, 2405–2411; b) K.-W. Cao, H.-Y. Sun, Q. Xue, Y. Ding, T.-J. Wang, F.-M. Li, G.-R. Xu, P. Chen, Y. Yang, Y. Chen, *ChemElectroChem* **2021**, *8*, 1759–1765.
[40] I. Suarez-Martinez, C. P. Ewels, X. Ke, G. Van Tendeloo, S. Thiess, W. Drube, A. Felten, J.-J. Pireaux, J. Ghijsen, C. Bittencourt, *ACS Nano* **2010**, *4*, 1680–1686.

[41] C.-C. Chang, C.-Y. Liu, S.-Y. Wu, M.-K. Tsai, *Phys. Chem. Chem. Phys.* **2017**, *19*, 4989–4996.
[42] a) A. B. Kroner, M. A. Newton, M. Tromp, A. E. Russell, A. J. Dent, J. Evans, *ChemPhysChem* **2013**, *14*, 3606–3617; b) F. Aguilera-Granja, J. L. Rodríguez-López, K. Michaelian, E. O. Berlanga-Ramírez, A. Vega, *Phys. Rev. B* **2002**, *66*, 224410; c) N. Karachi, M. Hosseini, Z. Parsaee, R. Razavi, *J. Photochem. Photobiol. A* **2018**, *364*, 344–354; d) C. Yang, Y. Cui, Y. Su, Y. Cheng, D. Yao, Y. Liao, S. Liu, Y. Fang, Y. Wu, X. Wang, Y. Song, G. Lu, Z. Li, *ACS Appl. Energy Mater.* **2023**, *6*, 6317–6326.
[43] H. Cheng, Y.-A. Zhu, D. Chen, P.-O. Åstrand, P. Li, Z. Qi, X.-G. Zhou, *J. Phys. Chem. C* **2014**, *118*, 23711–23722.
[44] a) H.-Y. Cheng, Y.-A. Zhu, P.-O. Åstrand, D. Chen, P. Li, X.-G. Zhou, *J. Phys. Chem. C* **2013**, *117*, 14261–14271; b) M. Narayanan Nair, M. Cranney, T. Jiang, S. Hajjar-Garreau, D. Aubel, F. Vonau, A. Florentin, E. Denys, M. L. Bocquet, L. Simon, *Phys. Rev. B* **2016**, *94*, 075427.
[45] F. Notheisz, A. Mastalir, M. Bartók, *J. Catal.* **1992**, *134*, 608–614.
[46] W. Li, L. Huang, M. C. Tringides, J. W. Evans, Y. Han, *J. Phys. Chem. Lett.* **2020**, *11*, 9725–9730.
[47] Y. Liu, X. Liu, C.-Z. Wang, Y. Han, J. W. Evans, A. Lii-Rosales, M. C. Tringides, P. A. Thiel, *J. Phys. Chem. C* **2021**, *125*, 6954–6962.
[48] Y. Han, A. Lii-Rosales, M. C. Tringides, J. W. Evans, P. A. Thiel, *Phys. Rev. B* **2019**, *99*, 115415.
[49] a) E. Castillejos, P.-J. Debouttière, L. Roiban, A. Solhy, V. Martinez, Y. Kihn, O. Ersen, K. Philippot, B. Chaudret, P. Serp, *Angew. Chem. Int. Ed.* **2009**, *48*, 2529–2533; b) Y. Wang, Z. Rong, Y. Wang, P. Zhang, Y. Wang, J. Qu, *J. Catal.* **2015**, *329*, 95–106.
[50] E. N. K. Glover, S. G. Ellington, G. Sankar, R. G. Palgrave, *J. Mater. Chem. A* **2016**, *4*, 6946–6954.
[51] a) T.-E. Hsieh, S. Maisel, H. Wittkämper, J. Frisch, J. Steffen, R. G. Wilks, C. Papp, A. Görling, M. Bär, *J. Phys. Chem. C* **2023**, *127*, 20484–20490; b) L. Guczi, G. Petö, A. Beck, Z. Pászti, *Top. Catal.* **2004**, *29*, 129–138.
[52] a) R. G. Rao, R. Blume, T. W. Hansen, E. Fuentes, K. Dreyer, S. Moldovan, O. Ersen, D. D. Hibbitts, Y. J. Chabal, R. Schlögl, J.-P. Tessonnier, *Nat. Commun.* **2017**, *8*, 340; b) R. Garg, N. K. Dutta, N. R. Choudhury, *Nanomaterials* **2014**, *4*, 267–300.
[53] L. Vanoye, B. Guicheret, C. Rivera-Cárcamo, J. Audevard, J. Navarro-Ruiz, I. del Rosal, I. C. Gerber, C. H. Campos, B. F. Machado, J. Volkman, R. Philippe, P. Serp, A. Favre-Réguillon, *J. Catal.* **2023**, *424*, 173–188.
[54] A. I. Frenkel, *Z. Kristallogr. - Cryst. Mater.* **2007**, *222*, 605–611.
[55] a) Y. Li, A. I. Frenkel, *Acc. Chem. Res.* **2021**, *54*, 2660–2669; b) S. Zhang, Y. Tang, L. Nguyen, Y. F. Zhao, Z. Wu, T. W. Goh, J. J. Liu, Y. Li, T. Zhu, W. Huang, *ACS Catal.* **2018**, *8*, 110–121; c) L. Nguyen, S. Zhang, L. Wang, Y. Li, H. Yoshida, A. Patlolla, A. I. TakedaFrenkel, F. Tao, *ACS Catal.* **2016**, *6*, 840–850; d) M. Kottwitz, Y. Li, H. Wang, A. I. Frenkel, R. G. Nuzzo *Chemistry-Methods* **2021**, *1*, 278–294.
[56] A. I. Frenkel *Chem. Soc. Rev.* **2012**, *41*, 8163–8178.
[57] a) Z. Duan, J. Timoshenko, P. Kunal, S. House, H. Wan, K. Jarvis, C. Bonifacio, J. C. Yang, R. M. Crooks, A. I. Frenkel, S. Humphrey, G. Henkelman, *Nanoscale* **2018**, *10*, 22520–22532; b) Y. Sun, A. I. Frenkel, R. Isseroff, C. Shonbrun, M. Forman, K. Shin, T. Koga, H. White, L. Zhang, Y. Zhu, M. H. Rafailovich, J. C. Sokolov, *Langmuir* **2006**, *22*, 807–816; c) Y. Li, A. I. Frenkel, *Acc. Chem. Res.* **2021**, *54*, 2660–2669.
[58] J. Ma, D. Alfè, A. Michaelides, E. Wang, *Phys. Rev. B* **2009**, *80*, 033407.
[59] A. V. Krasheninnikov, P. O. Lehtinen, A. S. Foster, R. M. Nieminen, *Chem. Phys. Lett.* **2006**, *418*, 132–136.
[60] J. Navarro-Ruiz, C. Rivera-Cárcamo, B. Machado, P. Serp, I. Del Rosal, I. C. Gerber, *ACS Appl. Nano Mater.* **2021**, *4*, 12235–12249.
[61] J. Guo, J. Lee, C. I. Contescu, N. C. Gallego, S. T. Pantelides, S. J. Pennycook, B. A. Moyer, M. F. Chisholm, *Nat. Commun.* **2014**, *5*, 5389.
[62] Y. Jinlong, F. Toigo, W. Kelin, *Phys. Rev. B* **1994**, *50*, 7915–7924.
[63] Z. Li, S. Li, Y. Xu, N. Tang, *Chem. Commun.* **2023**, *59*, 6286–6300.
[64] T. Wassmann, A. P. Seitsonen, A. M. Saitta, M. Lazzeri, F. Mauri, *Phys. Rev. Lett.* **2008**, *101*, 096402.
[65] A. M. Oyarzún, C. D. Latham, L. R. Radovic, P. R. Briddon, M. J. Rayson, *Phys. Chem. Chem. Phys.* **2018**, *20*, 26968–26978.
[66] a) K. Feng, H. Zhang, J. Gao, J. Xu, Y. Dong, Z. Kang, J. Zhong, *Appl. Phys. Lett.* **2020**, *116*; b) J. Finzel, K. M. Sanroman Gutierrez, A. S. Hoffman, J. Resasco, P. Christopher, S. R. Bare, *ACS Catal.* **2023**, *13*, 6462–6473.
[67] a) C. Rivera-Cárcamo, F. Leng, I. C. Gerber, I. del Rosal, R. Poteau, V. Collière, P. Lecante, D. Nechiyil, W. Bacsa, A. Corrias, M. R. Axet, P. Serp, *Catal. Sci. Technol.* **2020**, *10*, 4673–4683; b) Y. Zhang, D. T. Tran, D. Baker, S. Zhang, T. Wang, S. Hwang, E. Schulman, J. Fu, W. Zheng, D. G. Vlachos, J. Qi, P. Christopher, Y. Liu, A. Frenkel, D. Liu, *Mol. Catal.* **2022**, *531*, 112709.
[68] W. Tan, S. Xie, D. Le, W. Diao, M. Wang, K.-B. Low, D. Austin, S. Hong, F. Gao, L. Dong, L. Ma, S. N. Ehrlich, T. S. Rahman, F. Liu, *Nat. Commun.* **2022**, *13*, 7070.
[69] E. Auer, A. Freund, J. Pietsch, T. Tacke, *Appl. Catal. A: Gen.* **1998**, *173*, 259–271.
[70] D. Yang, P. Xu, N. D. Browning, B. C. Gates, *J. Phys. Chem. Lett.* **2016**, *7*, 2537–2543.
[71] M. G. Farpón, W. Henao, P. N. Plessow, E. Andrés, R. Arenal, C. Marini, G. Agostini, F. Studt, G. Prieto, *Angew. Chem. Int. Ed.* **2023**, *62*, e202214048.
[72] M. Tan, D. Wang, P. Ai, G. Liu, M. Wu, J. Zheng, G. Yang, Y. Yoneyama, N. Tsubaki, *Appl. Catal. A: Gen.* **2016**, *527*, 53–59.
[73] D. R. Aireddy, K. Ding, *ACS Catal.* **2022**, *12*, 4707–4723.
[74] P. Serp, *ChemCatChem* **2023**, *15*, e202300545.
[75] a) C. Rivera-Cárcamo, I. C. Gerber, I. del Rosal, B. Guicheret, R. Castro Contreras, L. Vanoye, A. Favre-Réguillon, B. F. Machado, J. Audevard, C. de Bellefon, R. Philippe, P. Serp, *Catal. Sci. Technol.* **2021**, *11*, 984–999; b) J. Audevard, J. Navarro-Ruiz, V. Bernardin, Y. Tison, A. Corrias, I. Del Rosal, A. Favre-Réguillon, R. Philippe, I. C. Gerber, P. Serp, *ChemCatChem* **2023**, *15*, e202300036.
[76] a) J. W. Gregory, S. D. Jackson, *React. Kinet. Mech. Catal.* **2021**, *133*, 669–686; b) Y. Zhao, Ö. D. Bozkurt, S. F. Kurtoğlu-Öztulum, M. Su Yordanli, A. S. Hoffman, J. Hong, J. E. Perez-Aguilar, A. Saltuk, D. Akgül, O. Demircan, T. A. Ateşin, V. Aviyente, B. C. Gates, S. R. Bare, A. Uzun, *J. Catal.* **2024**, *429*, 115196.
[77] S. Wang, T. Liu, Y. Zhu, X. Liu, Q. Luo, M. Zhu, T. Ding, T. Yao, *J. Phys. Chem. C* **2023**, *127*, 5911–5919.
[78] J. A. Alonso, M. J. López, *Phys. Chem. Chem. Phys.* **2022**, *24*, 2729–2751.
[79] A. Dutta, P. Mondal, *J. Phys. Chem. C* **2018**, *122*, 16925–16939.
[80] H. Jin, W. Song, C. Cao, *ACS Catal.* **2023**, *13*, 15126–15142.
[81] H. Wang, F. Shi, M. Pu, M. Lei, *ACS Catal.* **2022**, *12*, 11518–11529.
[82] a) H. Fu, H. Zhang, G. Yang, J. Liu, J. Xu, P. Wang, N. Zhao, L. Zhu, B. H. Chen, *New J. Chem.* **2022**, *46*, 1158–1167; b) J. Yang, L. Yang, L. Zhang, T. Yu, D. Zhai, H. Wang, W. Zhou, Y. Li, G. Ren, L. Sun, W. Deng, *Chem. Eur. J.* **2023**, *29*, e202203108.
[83] a) M. S. Ahmad, H. He, Y. Nishina, *Org. Lett.* **2019**, *21*, 8164–8168; b) Z. Luo, R. Nie, V. T. Nguyen, A. Biswas, R. K. Behera, X. Wu, T. Kobayashi, A. Sadow, B. Wang, W. Huang, L. Qi, *Nat. Commun.* **2020**, *11*, 4091; c) B. Li, Z. Xu, *J. Am. Chem. Soc.* **2009**, *131*, 16380–16382; d) X. Chen, Q. Shen, Z. Li, W. Wan, J. Chen, J. Zhang, *ACS Appl. Mater. Interf.* **2020**, *12*, 654–666; e) X. Huang, X. Zeng, X. Zhang, Z. Xie, *Phys. Chem. Chem. Phys.* **2022**, *24*, 28895–28902.
[84] H. Zhou, L. Shi, Q. Sun, *Chin. J. Catal.* **2012**, *33*, 1463–1469.
[85] A. Dasgupta, J. Matos, H. Muramatsu, Y. Ono, V. Gonzalez, H. Liu, C. Rotella, K. Fujisawa, R. Cruz-Silva, Y. Hashimoto, M. Endo, K. Kaneko, L. R. Radovic, M. Terrones, *Carbon* **2018**, *139*, 833–844.
[86] S. Wang, J. Dai, Z. Shi, Z. Xiong, Z. Zhang, S. Qiu, R. Wang, *ChemPlusChem* **2020**, *85*, 247–253.
[87] R. Franke, D. Selent, A. Börner, *Chem. Rev.* **2012**, *112*, 5675–5732.
[88] a) S. Hanf, L. Alvarado Rupflin, R. Gläser, S. A. Schunk, *Catalysts* **2020**, *10*, 510; b) S. Tao, D. Yang, M. Wang, G. Sun, G. Xiong, W. Gao, Y. Zhang, Y. Pan, *iScience* **2023**, *26*, 106183.
[89] Q. Yang, P. Wang, C. Li, B. Wang, Y. Zheng, Y. Feng, Z. Miao, M. Li, M.-Y. Wang, S. Huang, X. Ma, *Chem. Eng. J.* **2024**, *481*, 148529.
[90] a) B. Li, X. Li, K. Asami, K. Fujimoto, *Energy Fuels* **2003**, *17*, 810–816; b) G. Snyder, A. Tadd, M. A. Abraham, *Ind. Eng. Chem. Res.* **2001**, *40*, 5317–5325; c) T. Li, F. Chen, R. Lang, H. Wang, Y. Su, B. Qiao, A. Wang, T. Zhang, *Angew. Chem. Int. Ed.* **2020**, *59*, 7430–7434; d) X. Wei, Y. Jiang, Y. Ma, J. Fang, Q. Peng, W. Xu, H. Liao, F. Zhang, S. Dai, Z. Hou, *Chem. Eur. J.* **2022**, *28*, e202200374.
[91] J. Amsler, B. B. Sarma, G. Agostini, G. Prieto, P. N. Plessow, F. Studt, *J. Am. Chem. Soc.* **2020**, *142*, 5087–5096.
[92] a) C. G. Arena, D. Drago, F. Faraone, *J. Mol. Catal. A: Chemical* **1999**, *144*, 379–388; b) B. Zhang, D. Peña Fuentes, A. Börner, *ChemTexts* **2021**, *8*, 2.
[93] Y.-Q. Su, L. Zhang, Y. Wang, J.-X. Liu, V. Muravev, K. Alexopoulos, I. A. W. Filot, D. G. Vlachos, E. J. M. Hensen, *npj Comput. Mater.* **2020**, *6*, 144.
[94] B. Liu, Y. Wang, N. Huang, X. Lan, Z. Xie, J. G. Chen, T. Wang, *Chem* **2022**, *8*, 2630–2658.
[95] E. Zuidema, E. Daura-Oller, J. J. Carbó, C. Bo, P. W. N. M. van Leeuwen, *Organometallics* **2007**, *26*, 2234–2242.
[96] M. Tan, G. Yang, T. Wang, T. Vitidsant, J. Li, Q. Wei, P. Ai, M. Wu, J. Zheng, N. Tsubaki, *Catal. Sci. Technol.* **2016**, *6*, 1162–1172.

[97] W. Shang, B. Qin, M. Gao, X. Qin, Y. Chai, G. Wu, N. Guan, D. Ma, L. Li, *CCS Chem.* **2023**, *5*, 1526–1539.
[98] P. Qi, J. Wang, X. Djitcheu, D. He, H. Liu, Q. Zhang, *RSC Adv.* **2022**, *12*, 1216–1227.
[99] a) S. Xiang, P. Huang, J. Li, Y. Liu, N. Marcella, P. K. Routh, G. Li, A. I. Frenkel, *Phys. Chem. Chem. Phys.* **2022**, *24*, 5116–5124; b) X. Liu, L. Zheng, C. Han, H. Zong, G. Yang, S. Lin, A. Kumar, A. R. Jadhav, N. Q. Tran, Y. Hwang, J. Lee, S. Vasimalla, Z. Chen, S.-G. Kim, H. Lee, *Adv. Funct. Mater.* **2021**, *31*, 2100547.
[100] T. Placke, V. Siozios, S. Rothermel, P. Meister, C. Colle, M. Winter, *Z. fur Phys. Chem.* **2015**, *229*, 1451–1469.
[101] B. Ravel, M. Newville, *J. Synchrotron Rad.* **2005**, *12*, 537–541.
[102] J. J. Rehr, R. C. Albers, *Rev. Mod. Phys.* **2000**, *72*, 621–654.
[103] a) G. Kresse, J. Furthmüller, *Phys. Rev. B* **1996**, *54*, 11169–11186; b) G. Kresse, J. Furthmüller, *Comput. Mater. Sci.* **1996**, *6*, 15–50.
[104] J. P. Perdew, K. Burke, M. Ernzerhof, *Phys. Rev. Lett.* **1996**, *77*, 3865–3868.
[105] S. Grimme, J. Antony, S. Ehrlich, H. Krieg, *J. Chem. Phys.* **2010**, *132*.
[106] a) P. E. Blöchl, *Phys. Rev. B* **1994**, *50*, 17953–17979; b) G. Kresse, D. Joubert, *Phys. Rev. B* **1999**, *59*, 1758–1775.
[107] H. J. Monkhorst, J. D. Pack, *Phys. Rev. B* **1976**, *13*, 5188–5192.
[108] G. Makov, M. C. Payne, *Phys. Rev. B* **1995**, *51*, 4014–4022.

Manuscript received: February 19, 2024
Accepted manuscript online: June 25, 2024
Version of record online: August 19, 2024